Tutors

Dr. David Curcó Cantarell
Departament d'Enginyeria Química i Química Analítica

Dr. Ricard Torres Castillo
Departament d'Enginyeria Química i Química Analítica

Grau en Enginyeria Química

Treball Final de Grau

Effects of incorporating baffles into the cooling system of an internal combustion engine. Study through ANSYS® CFD software.

Adrián Fernández Córdoba

January 2021

UNIVERSITAT DE BARCELONA

Aquesta obra està subjecta a la llicència de:
Reconeixement–NoComercial-SenseObraDerivada

http://creativecommons.org/licenses/by-nc-nd/3.0/es/

Le mieux est l'ennemi du bien
Voltaire

Li vull donar les gràcies a en Mateu per acompanyar-me en el meu projecte vital i per fer-me la vida tan fàcil i tan agradable. A més, sense el teu exemple no crec que m'hagués atrevit endinsar-me en aquest segon grau tan enriquidor alhora que exigent que m'ha portat al límit alhora que m'ha fet gaudir moltíssim aprenent com funciona el món.

També li estic molt agraït a en Ricard i a en David, els meus tutors en aquest treball, per acceptar-ne la tutorització tot i anar tan enfeinats. Les nostres freqüents i extenses reunions filosofant sobre molts dels aspectes continguts en aquest treball m'han ajudat molt, tant pels consells científics i de redacció, com pels ànims que m'heu donat, potser sense adonar-vos, amb les vostres bones paraules sobre la meva feina.

Per últim vull pronunciar un agraïment general per tots els professors que he tingut no només al grau d'enginyeria sinó també al grau de química. He gaudit molt i après molt a les vostres classes durant els tretze semestres que ha durat aquest viatge. Sense cap mena de dubte m'heu convertit en una persona més sabia i moltíssim més rigorosa que aquell noi de 18 anys que va entrar ple d'il·lusió a la facultat el juliol del 2014.

CONTENTS

SUMMARY i

RESUM iii

1. INTRODUCTION 1

1.1. INTERNAL COMBUSTION ENGINES 1

1.1.1. Anatomy of an internal combustion engine 2

1.1.1.1. ICE cooling systems 3

1.1.2. Present and future of the internal combustion engine 6

1.2. COMPUTATIONAL FLUID DYNAMICS 7

1.2.1. CFD applications on ICE design 8

1.2.2. Governing equations 8

1.2.2.1. Transport equations 8

1.2.2.2. Turbulence models 10

1.2.3. ANSYS® Fluent® CFD software 12

2. OBJECTIVES 15

3. MATERIALS AND METHODS 17

3.1. HARDWARE AND SOFTWARE USED 17

3.2. PREPROCESSING 17

3.2.1. Model design 17

3.2.2. Meshing 20

3.3. SIMULATION SETUP 23

3.3.1. General setup 23

3.3.2. Transport and viscous models 24
3.3.3. Materials 24
3.3.4. Boundary conditions 25
3.3.4.1. Inlet 25
3.3.4.2. Outlet 26
3.3.4.3. Inner wall 27
3.3.4.4. Outer wall 28
3.3.4.5. Other walls 28
3.3.5. Solution setup 29
3.3.5.1. Solution methods 29
3.3.5.2. Solution controls 29
3.3.5.3. Solution initialization 30
3.4. POSTPROCESSING 30
3.4.1 ANSYS® Fluent® Solution reports 30
3.4.2 ANSYS® CFD-Post reports 32
4. SIMULATION RESULTS AND DISCUSSION 33
4.1. SIMULATIONS ON SMOOTH COOLING JACKETS 33
4.1.1. Part load scenario 33
4.1.1.1. Mesh validation 33
4.1.1.2. Results 34
4.1.2. Full load scenario 36
4.1.2.1. Mesh validation 36
4.1.2.2. Results 37
4.2. SIMULATIONS ON ENHANCED COOLING JACKETS 40
4.2.1. Models 40
4.2.2. Mesh validation 41

4.2.3. Results 42
5. CONCLUSIONS 51
6. FUTURE WORK 53
REFERENCES AND NOTES 55
ACRONYMS 59

APPENDICES 61
APPENDIX 1: THERMOPHYSICAL PROPERTIES OF EG-W MIXTURES 63
APPENDIX 2: OTHER VIEWS OF THE ENHANCED COOLING JACKETS 67
APPENDIX 3: DISCARDED PROTOTYPES 69

SUMMARY

As of 2021, even with growing concerns about climate change, internal combustion engines still power more than 99% of the vehicles on the planet, from the smallest of motorcycles to the largest container ships. Internal combustion engines are thermal machines subject to great irreversibilities that have peak thermal efficiencies well below 50% and thus reject large amounts of heat. As a consequence of this, they require cooling to keep their temperature below the maximum service temperature of their constitutive materials. In most modern engines, cooling is achieved through the forced circulation of a liquid coolant through the engine. The homogeneity of this refrigeration is critical as uneven cooling creates great thermal stresses that would severely reduce the durability and reliability of the engine.

In this work, the cooling jacket of the cylinder on an internal combustion engine was modelized and analyzed through computational fluid dynamics simulations using the academic version of the commercial software ANSYS® Fluent®. First, a simplified model based on the cooling jacket on a single-cylinder liquid-cooled 125 cc spark-ignited engine was elaborated and validated through comparison with data available in the literature. Boundary conditions were obtained from a combination of experimental and literature data and the academic version of ANSYS® Fluent® proved being sufficient to perform a semiquantitative analysis. Once its results were validated, this system was then modified by including different combinations of baffles and additional outlets with the aim of improving its heat transfer characteristics, especially in terms of cooling homogeneity.

Results were especially promising for the system containing the combination of additional outlets on the top part of the cooling jacket and a baffle on its outer wall. Uniform and enhanced cooling was achieved in the area of influence of the baffle while a notable pressure drop reduction in the cooling jacket was attributed to the presence of the additional outlets.

Keywords: computational fluid dynamics, CFD, internal combustion engine, ICE, cooling, hotspots, ANSYS®, Fluent®.

RESUM

Al 2021, fins i tot amb la preocupació creixent sobre el canvi climàtic, els motors de combustió interna segueixen alimentant més del 99 % dels vehicles del planeta. Els motors de combustió interna són màquines tèrmiques sotmeses a irreversibilitats que tenen eficiències tèrmiques per sota del 50 % i que, per tant, requereixen de refrigeració per protegir la integritat dels seus materials. En la majoria dels motors moderns, la refrigeració s'aconsegueix mitjançant la circulació forçada d'un líquid refrigerant pel motor. L'homogeneïtat d'aquesta refrigeració és fonamental, ja que una refrigeració desigual crearia tensions tèrmiques que reduirien considerablement la durabilitat i fiabilitat del motor.

En aquest treball, la camisa de refrigeració del cilindre d'un motor de combustió interna s'ha modelitzat i analitzat a través de simulacions de dinàmica de fluids computacional emprant la versió acadèmica del programari comercial ANSYS® Fluent®. En primer lloc, s'ha elaborat i validat amb dades bibliogràfiques un model simplificat basat en la camisa de refrigeració d'un motor de gasolina monocilíndric de 125 cc refrigerat per líquid. Les condicions de contorn s'han obtingut a partir d'una combinació de dates experimentals i bibliogràfiques i la versió acadèmica d'ANSYS® Fluent® ha demostrat ser suficient per realitzar una anàlisi semiquantitativa del sistema tractat. Un cop validat, aquest model s'ha modificat per incloure-hi diferents combinacions de deflectors i sortides addicionals amb l'objectiu de millorar les seves característiques en termes de transferència de calor, especialment pel que fa a l'homogeneïtat de la refrigeració.

Els resultats obtinguts són especialment prometedors pel sistema equipat amb sortides addicionals a la part superior de la camisa de refrigeració i un deflector a la seva paret exterior. En aquest model s'ha aconseguit una refrigeració intensa i uniforme de l'àrea d'influència del deflector mentre que a la presència de sortides addicionals se li pot atribuir una considerable disminució de les pèrdues de càrrega a la camisa de refrigeració.

Paraules clau: dinàmica de fluids computacional, CFD, motor de combustió interna, refrigeració, punts calents, ANSYS®, Fluent®.

1. INTRODUCTION

In the past, the design and development of internal combustion engines was a complex, slow and costly process that was based on the construction of prototypes. Today, the advances in technology both in the hardware and software fields allow for rapid prototyping through computational simulations, with only the best and most refined candidates being actually built and physically tested.

1.1. INTERNAL COMBUSTION ENGINES

Even under increasingly stricter regulations, as of 2021, internal combustion engines (ICEs) still remain as the primary source of energy for automotive applications ranging from small motorcycles with a power output of a few kW to large container ships with close to a hundred MW of usable output power. ICEs are heat engines that generate work from the expansion of hot gasses produced by the combustion of a fuel inside an enclosed chamber. The hot side of the thermal machine is located inside of it and hence its name.

Several variations have been introduced since its inception in the beginning of the 19th century, the most commonly used in land transportation today being the spark-ignition reciprocating engine running on the Otto cycle (gasoline, gas or petrol engine) and the compression-ignition reciprocating engine running on the Diesel cycle (diesel engine). Both cycles rely on the same four-step (or stroke) elemental process based on intake-compression-combustion-exhaust with the only difference being that gasoline engines compress a mixture of fuel and air and diesel engines compress only air, with fuel being added later. Another main successful type of internal combustion machines are turbine engines. Their operation is based on the Brayton thermodynamic cycle and they found widespread use in aircraft, where their high specific power and power density makes them the most suitable alternative [1].

To continue existing in a world increasingly aware of climate change consequences, ICEs must constantly increase in efficiency, reliability and exhaust gas stream purification. However,

since ICEs are heat engines, improvements in efficiency are virtually limited by the Carnot efficiency (see equation 1), which is a consequence of the second law of thermodynamics which, in one of its formulations, states that heat energy cannot be completely converted into usable work [2].

$$\eta_{max} = 1 - \frac{T_C}{T_H} \quad (1)$$

Where η_{max} is the maximum thermal efficiency for the heat engine ("Carnot's efficiency"), T_C is the temperature of the cold side of the machine (heat sink) and T_H the temperature of its hot source. In practice however, the irreversibilities present on real engines (friction losses, fluid pressure drops, etc.) and engineering constraints such as required power density, output power, cost, etc. further lower the maximum thermal efficiency to around 30% and 45% for commercially available automotive Otto and Diesel cycle engines, respectively [3].

1.1.1. Anatomy of an internal combustion engine

The main components of an internal combustion engine are its combustion chamber, piston and spark plug (only in spark-ignited engines) (see figure 1). Combustion and extraction of work energy can only take place if these elements are present. The rest of components are present to allow for the safe and sustained operation of the engine to take place: poppet type valves opened by the action the camshaft and closed by springs control the flux of gasses from and to the combustion chamber. Useful work in the form of rotational movement is extracted from the reciprocal movement of the piston thanks to the connecting rod and the crankshaft. And finally, metal on metal contact of rapidly moving parts is possible thanks to the lubrication provided by the oil contained in the crankcase and propelled throughout the engine by the oil pump.

As it can be inferred from the Carnot's efficiency definition (see section 1.1), the higher the temperature on the combustion chamber of an internal combustion engine (hot source) the higher its attainable thermal efficiency can be (considering that the cold side, the atmosphere, remains at constant temperature). Materials and lubricants, however, limit the maximum operation temperature of the engine which needs to be controlled by means of a cooling system [4].

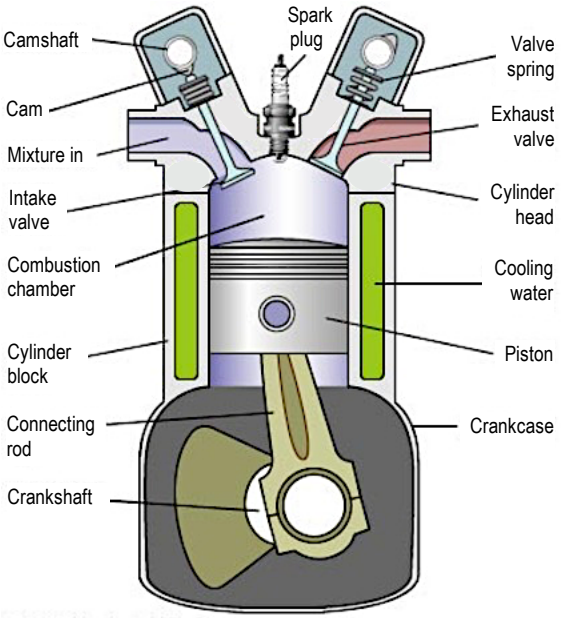

Figure 1. Cross section of a single-cylinder liquid-cooled internal combustion engine. Adapted from "Britannica: Internal Combustion Engine" [Online]. Available: https://www.britannica.com/technology/internal-combustion-engine. [Accessed 2 January 2021].

1.1.1.1. ICE cooling systems

The cooling system is one of the indispensable auxiliary parts of an internal combustion engine. With cylinder wall heat fluxes of up to 10 MW/m^2 [1], if an engine were to be operated in the absence of any kind of cooling, it would only have the specific heat of its own materials as a thermal management aid and would soon fail catastrophically due to overheating. Although detrimental to thermal efficiency, some form of heat extraction is needed in order to prevent engine failure.

Heat transfer is not only required to make engine operation possible; it also greatly affects engine performance and exhaust emissions. For example, higher than optimal temperatures can cause cylinder wall oil film burning, preignition of the air-fuel mixture and nitrogen oxides

emissions (NO_X). On the other hand, lower than optimal engine temperatures may also cause problems such as a deterioration in engine thermal efficiency (as previously stated), poor lubrication due to higher oil viscosity and the emission of unburnt fuel (hydrocarbon emissions) [1]. For these reasons, since their inception internal combustion engines have always been fitted with some form of cooling, either active or passive.

Early engines were directly cooled by ambient air with the help of surface extending devices: cooling fins. The main advantage of this technology was its simplicity: no moving parts are involved as the movement of the vehicle provides the required airflow to the cooling fins. Their simplicity also causes most of their disadvantages: cooling is directly related to vehicle speed rather than to engine load which can lead to over or undercooling. Moreover, hotspots can develop on areas subject to large heat loads and the engine must be exposed to direct airflow which has a negative impact on aerodynamics and limits engine layout possibilities. Nonetheless, today air cooling still remains the system of choice in low-cost small engined motorcycles and in most of aircraft engines (either piston or turbine-based) where none of the beforementioned disadvantages are present due to an unrestricted and constant airflow [5].

Later developments in engine technology allowed for the construction of engines with multiple adjacent cylinders arranged in complex layouts and a higher specific output which proved difficult to cool using air. In the first decades of the 20th century, thermosyphon liquid cooling was introduced in automobiles such as the Ford Model T (1909 - 1927) which used a radiator and a radiator fan, but no fluid circulation aids in pro of simplicity and reliability. The liquid cooling allowed for refrigeration of internal areas of the engine such as between the cylinders and homogenized temperatures thus reducing thermal stresses. However, the performance of such systems was limited by its design (natural convection) and they were abandoned in favor of forced convection liquid cooling systems [6].

Modern engines use a forced convection liquid-based setup typically containing, at least, a radiator, a radiator fan, a centrifugal pump and a thermostat (see figure 2). The cooling fluid circulates with the aid of the pump through the cooling jackets and passages of the engine extracting heat to then be cooled down at the radiator to repeat the cycle. When airflow through the radiator is insufficient for the cooling demands of the engine, such as when travelling uphill in a heavily loaded vehicle, an electrically power fan may be activated.

Since the cooling capacity of the system is linked to engine speed (the pump is mechanically driven by engine) and not engine load, cooling capacity is regulated by the thermostat: a passive temperature regulated valve, that controls the amount of coolant that is directed to the radiator for heat extraction. The addition of the thermostat ensures that the heat extracted from the engine matches its cooling needs at all time preventing under or overcooling and allowing the engine to quickly reach its optimal operating temperature upon startup, when no coolant is directed to the radiator [7].

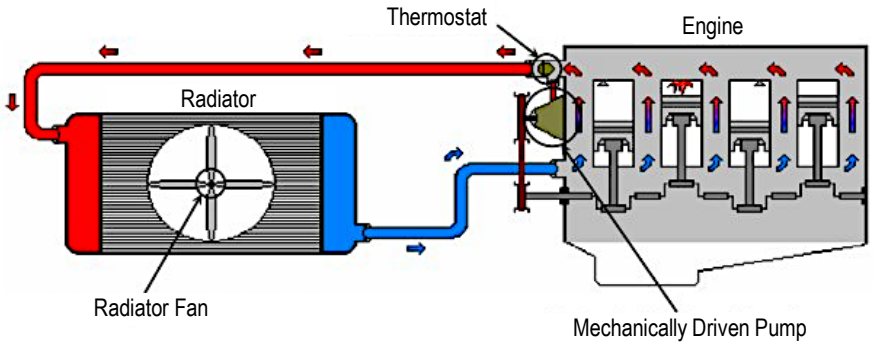

Figure 2. Typical layout for the cooling system of a modern liquid-cooled internal combustion engine. Adapted from the work of Mitchell et al. [7].

The use of forced convection liquid cooling provides the best heat transfer performance among the systems described in this work thanks to the high heat transfer coefficient that can be attained by the forced circulation (high turbulence) of a liquid (high density and heat capacity). This allows for uniform and controlled temperatures to be attained for all engine parts, minimizing the hotspot presence which could greatly reduce engine life expectancy due to thermal stresses. High temperature areas can also cause preignition (uncontrolled combustion) in spark-ignited engines [7].

The most common cooling fluid used in ICEs is a mixture of water (W) and ethylene glycol (EG) with the addition of preservatives and corrosion inhibitors [8]. The presence of such glycol [figure 3, left] allows for a depression of the freezing point of -37 ºC (to prevent engine damage in cold climates) and the rise of the normal boiling point to 108 ºC in mixtures with a 50% by volume content of EG [9].

Since higher engine temperatures provide enhanced thermal efficiency (see section 1.1) cooling systems are pressurized to further increase the boiling point of the coolant mixtures and allow for operation at higher temperatures, with relative pressures above 2 bar being increasingly common (see figure 3, right) [10].

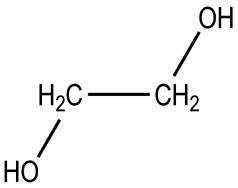

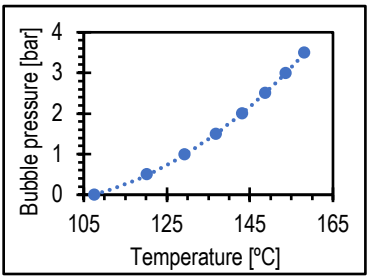

Figure 3. Ethylene glycol semi developed structure (left) and relative bubble pressure as a function of temperature for a 50% $^{V}/_{V}$ EG-W mixture (right, see appendix 1 for more information). Own work.

1.1.2. Present and future of the internal combustion engine

Under the threat of highly efficient battery-powered fully electric powertrains current ICE developments focus on increasing thermal efficiency and thus reducing fuel consumption without affecting reliability or emissions.

In the short term, while electric powertrains gain momentum, current developments include the use of electric-thermal hybrid powertrains that allow the deactivation of the internal combustion engine in situations where its efficiency is compromised such as city driving [11] while other technologies are based on the use more of efficient aerodynamics and transmissions (i.e., with more gears or lower friction losses) or enhanced versions of the classical thermodynamical cycles such as the Atkinson cycle [12].

Due to its cost effectiveness, in recent years, one of the main techniques that manufacturers have used for the reduction of fuel consumption has been the use of engine downsizing [13]. Downsizing consists on the use of a smaller displacement engine so that friction and heat losses are lower due to its reduced size and then applying turbocharging and/or supercharging techniques to regain the power output lost in the miniaturization process. As it can be deduced, a smaller engine producing the same output power will require more intensive cooling to ensure

that the expected levels of reliability and durability are met [13]. Since less area is available for cooling on a downsized engine, efforts must be made in order to obtain a high and uniform heat transfer coefficient to prevent overheating and to avoid the appearance of hotspots.

A first approach to the enhancement of the cooling system for downsized engines can be based on computational fluid dynamics simulations in a similar manner as will be done in this work. By using this approach, the cost of the development of downsized engines can be minimized due to a reduction in the number of unsuccessful prototypes built to attain a certain degree of improvement.

1.2. COMPUTATIONAL FLUID DYNAMICS

In recent years computational fluid dynamics (CFD) has experienced a quick development mainly due to the progress in the computing power both in desktop computers and supercomputers. As its name implies, CFD is based on the solution of fluid dynamics problems computationally, allowing for the accurate description of complex phenomena taking place in large domains such as the atmosphere in meteorology or an aircraft in aeronautical engineering.

The possibilities of CFD are immense, with simulations usually taking the place that was formerly occupied by expensive and time-consuming experimentation. It founds applications in fields such as chemical engineering (fluid flow, heat transfer, chemical reactors...), environmental engineering (pollutant dispersion...), mechanical engineering (engine and combustion analysis, aerodynamics...) or physics (meteorological predictions...).

CFD, however, is based on mathematical models that are applicable only over a limited range of conditions and its results must be, at some point, validated through experimental data. Nonetheless, CFD is still a powerful tool, especially when applying modifications to an existing system (the code can be validated on experimental data from the original system) or when making first steps with novel configurations (where larger relative errors could be acceptable) [14].

As opposed to the classical engineering approach, where a single set of equations is solved in order to calculate the results, in computational fluid dynamics the system is divided into finite elements (it is meshed) and then a set of equations (microscopic balances, see section 1.2.2.) is solved for each of the generated elements with the aid numerical methods. Analytical CFD,

where only a single set of microscopic balances is solved also exists, but its application is severely limited to simple geometries due to the small range of differential equations that can be solved symbolically [15].

1.2.1. CFD applications on ICE design

As suggested in previous sections, due to the complex nature of ICEs, CFD can be a useful tool in early testing of changes and improvements in most of the areas concerned in ICE design. To cite some examples, Chadwell et al. [16] were able to improve the high load thermal efficiency of a downsized engine using a novel intake valve cooling setup through combustion simulations. Mashkour et al. [17] obtained heat transfer coefficients for combustion gasses to cylinder wall and exhaust manifold to air using ANSYS® that were later validated using experimental data found on the literature. Chun et al. [18] studied the effect of the addition of ring-shaped baffles on the intake valves of an ICE to promote air-fuel mixture swirl and improve engine thermal efficiency while reducing particulate emissions (soot).

Lastly, in strong relation with this work, Shingare et al. [19] created a model of the cooling system on a 4-cylinder generator using ANSYS® Fluent® and then validated their results experimentally showing that the model was accurate to the real engine in terms of temperatures and heat fluxes. Their accurate model was then used to assay the effect that the use of different engine coolant formulations and flow rates had on the temperature profile developed in the cooling jacket of the cylinders.

1.2.2. Governing equations

As previously stated, in computational fluid dynamics microscopic balances are solved either analytically or, most commonly, numerically (as in this work) for all the elements that compose the macroscopic system.

1.2.2.1 Transport equations

To fully describe a system, transport equations for mass, momentum and energy must be solved. The three equations have a vectorial character and share the same basic terms: accumulation in time, transport and generation. Some authors such as A. W. Date [20] describe these transport phenomena using one formal equation with different variables, highlining that all

transport phenomena can be modeled in a similar way (see equation 2). This parallelization was conceived in the mid 20th century by Bird et al [15] who are considered the fathers of unified transport phenomena as we know them today.

$$\underbrace{\frac{\partial(\rho\,\Phi)}{\partial t}}_{\text{Accumulation}} + \underbrace{\nabla\cdot(\rho\,\vec{v}\,\Phi)}_{\text{Advective Transport}} = \underbrace{\nabla\,[\Gamma_{eff}\,\nabla\Phi\,]}_{\text{Diffusive Transport}} + \underbrace{S_{\Phi}}_{\text{Generation}} \tag{2}$$

Where Φ is the variable subject to study (such as mass or momentum) and Γ_{eff} is its transport related property (such as viscosity or thermal conductivity). "·" indicates vectorial product. In this section, a brief review of the equations solved by the commercial simulator used in this work (ANSYS® Fluent®) will be performed [21].

General mass transport equation:

$$\frac{\partial\rho}{\partial t} + \nabla\cdot(\rho\,\vec{v}) = S_m \tag{3}$$

Where ρ is the density, t the time, $\vec{v}$ the velocity vector and S_m the mass generation term, which can account for mass added from another phase or true mass generation in nuclear reactions.

General momentum transport equation:

$$\frac{\partial}{\partial t}(\rho\,\vec{v}) + \nabla\cdot(\rho\,\vec{v}\,\vec{v}) = -\nabla P + \nabla\cdot(\bar{\bar{\tau}}) + \rho\vec{g} + \vec{F} \tag{4a}$$

Where P is the static pressure, $\rho\vec{g}$ is the gravitational force, $\vec{F}$ are the net external forces and $\bar{\bar{\tau}}$ is the stress tensor on the fluid:

$$\bar{\bar{\tau}} = \mu\left\{(\nabla\vec{v} + \nabla\vec{v}^{T}) - \frac{2}{3}\nabla\cdot\vec{v}\,I\right\} \tag{4b}$$

Where μ is the molecular viscosity, $\vec{v}^{T}$ the transposed velocity vector and I the unit tensor (the last term of the equation accounts for the effect of volume dilation). For Newtonian fluids the equation 4a can be simplified and expressed in terms of viscosity as follows:

$$\frac{\partial}{\partial t}(\rho \vec{v}) + \nabla\cdot(\rho \vec{v} \vec{v}) = -\nabla P + \mu_{eff} \nabla^2 \vec{v} + \rho\vec{g} + \vec{F} \quad (4c)$$

Where μ_{eff} is the combination of the molecular viscosity (μ, a fluid characteristic) and turbulent viscosity (μ_T, a flow characteristic) to take into account the effect of turbulence on the momentum transport [15].

General energy transport equation:

$$\frac{\partial}{\partial t}(\rho E) + \nabla \cdot \{\vec{v}(\rho E + P)\} = \nabla \cdot \left\{ k_{eff}\nabla T - \sum_j h_j \vec{J}_j + (\bar{\bar{\tau}}_{eff}\cdot\vec{v}) \right\} + S_h \quad (5a)$$

Where k_{eff} is the effective conductivity ($k + k_{turb}$), $\vec{J}_j$ is the diffusion flux of species j, h is their relative enthalpy and S_h is the heat generation term. The terms on the left side account for accumulation and advective transport while the right-hand-side terms represent energy transfer due to conduction, species diffusion and viscous dissipation. E is energy and is defined as:

$$E = h - \frac{P}{\rho} + \frac{v^2}{2} \quad (5b)$$

Where h is the sensible relative enthalpy and v is speed (the modulus of the velocity vector).

1.2.2.2. Turbulence models

Turbulence models are used to ultimately calculate the turbulent viscosity (and subsequently all other turbulent magnitudes) and solve the transport equations reviewed in the previous subsection taking into account the effects of turbulence. Turbulence itself is a complex and highly random phenomenon, making its precise definition very difficult. Since it is involved in most industrial flows, its modelization is a very active research topic as it can severely reduce engineering costs by use the simulations [22]. In this work the Realizable k-epsilon (k-ε) turbulence model contained in the ANSYS® Fluent® CFD software was used (see section 3.3.2). The term "realizable" arises from the satisfaction of certain mathematical constraints that are out of the scope of this work.

The Realizable k-ε model is a two-parameter semi-empirical turbulence model with k being the turbulence kinetic energy and ε its rate of dissipation. These two parameters are calculated based on their own transport equations [21] and are later used to calculate μ_T:

$$\frac{\partial}{\partial t}(\rho k) + \frac{\partial}{\partial x_j}(\rho k v_j) = \frac{\partial}{\partial x_j}\left[\left(\mu + \frac{\mu_T}{\sigma_k}\right)\frac{\partial k}{\partial x_j}\right] + G_k + G_b + \rho \varepsilon - Y_M + S_k \quad (6)$$

$$\frac{\partial}{\partial t}(\rho \varepsilon) + \frac{\partial}{\partial x_j}(\rho \varepsilon v_j) = \frac{\partial}{\partial x_j}\left[\left(\mu + \frac{\mu_T}{\sigma_\varepsilon}\right)\frac{\partial \varepsilon}{\partial x_j}\right] + \rho C_1 S \varepsilon - \rho C_2 \frac{\varepsilon^2}{k + \sqrt{\varepsilon \mu / \rho}} + C_{1\varepsilon}\frac{\varepsilon}{k} C_{3\varepsilon} G_b + S_\varepsilon \quad (7)$$

Where G_k represents the generation of turbulent kinetic energy due to velocity gradients, G_b the generation of turbulent kinetic energy due to buoyancy and Y_M the contribution of the fluctuating dilatation in compressible turbulence. C_2 and $C_{1\varepsilon}$ are constants, σ_k and σ_ε are the turbulent Prandtl numbers for k and ε and S_k and S_ε are their user generation terms. C_1 and S on equation 7 are defined as:

$$C_1 = \max\left[0.43, \frac{\eta}{\eta + 5}\right] ; S = \sqrt{2 S_{ij}^2} \quad \text{where} \quad \eta = S \frac{k}{\varepsilon} \quad (7b)$$

Finally, with values for the k and ε, the turbulent (or Eddy) viscosity can be computed from:

$$\mu_T = \rho C_\mu \frac{k^2}{\varepsilon} \quad (8)$$

Where C_μ is not a constant as in the Standard k-ε model but a parameter that takes into account rotation and angular velocity of the velocity field [21].

An important aspect of turbulence modelization is wall treatment. Without further sophistication, the Realizable k - ε does not accurately describe the near wall regions and the near wall fluid conditions are only vaguely estimated to save computational power [21]. In simulations where the near wall turbulence may play an important role (such as in this work) some form of near-wall treatment, must be used. The proximity to the walls of the system is defined through a variable called y+ (wye-plus), an adimensional stress dependent distance (see equation 9 and figure 4).

$$y^+ = \frac{\rho v_t y}{\mu} \quad \text{with} \quad v_t = \sqrt{\frac{\tau_w}{\rho}} \quad (9)$$

Where v_t is the friction velocity, y the distance to the wall and τ_w the wall shear stress. There are two main approaches to near wall treatment [21]: the wall function approach and the near-wall modelling. With wall functions, the viscous sublayer and the buffer layer (see figure 4)

are described by semiempirical formulas (wall-functions) without further modification of the turbulence model whereas with near-wall modelling the turbulent transport equations are modified in order to take into account the presence of the systems walls. If the mesh near the wall is sufficiently fine (first node at $y^+ \simeq 1$) both approaches should provide comparable results [21].

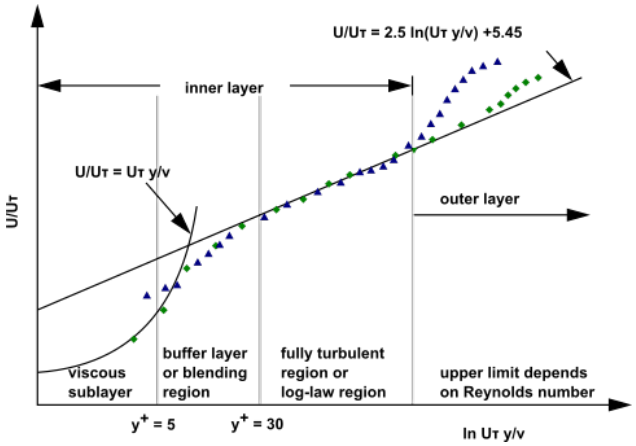

Figure 4. Adimensional speed (v/v_T) versus adimensional distance from wall (y^+) profile and its classical divisions in terms of y^+. Note that in this representation fluid speed is denoted as U. Extracted from the ANSYS® Fluent® Theory Guide [21].

1.2.3. ANSYS® Fluent® CFD software

ANSYS® is a multiphysics finite element simulation software developed by Swanson **An**alysis **Sys**tems Inc., a technology company founded in 1970. Over the years it has expanded its working fields either by internal research and development or by the acquisition of external software developed by third parties. All but its earliest versions have relied on a user-friendly graphic interface that has allowed researchers without special programming skills to run complex CFD simulations [23].

In 2006 it acquired Fluent Inc., a company centered in finite element simulation of fluid flow, heat and mass transfer and other related phenomena such as turbulence modelization which further broadened the applications of their simulation suite [24].

The ANSYS® simulation suite is centralized on the "ANSYS® Workbench™" application which provides a unified starting point and interface for all the software in the ANSYS®

engineering suite. For an ANSYS® Fluent® fluid flow simulation, the Workbench™ components required to have a complete simulation are geometry, meshing, setup, solution and results (see table 1). These fields are usually completed in the stated order although updating upstream components is possible (and common) when applying changes to existing simulations.

Table 1. Description of the Workbench™ components for an ANSYS® Fluent® fluid flow simulation.

Component	Description
Geometry	The geometry of the system is defined using one of the available ANSYS®-integrated CAD software or by importing it from an external file.
Meshing	The system is divided in finite elements for its analysis on the Meshing™ application. Local and global meshing tools are available.
Setup	The materials, boundary conditions and solving strategies are defined in the Fluent® software.
Solution	The results of the simulation are presented on the ANSYS® Fluent® application. Graphical representations and animations are available.
Results	Further analysis of the results can be performed on the ANSYS®-integrated software CFD-Post.

2. OBJECTIVES

The aim of this work is to suggest topology changes in the cooling jacket of a single cylinder internal combustion engine to enhance its heat transfer characteristics using computational fluid dynamics simulations. To achieve this main objective, three subobjectives must be attained:

- Learn how to use the commercial CFD simulation software ANSYS® Fluent® and gain sufficient skill with it to guarantee the accomplishment of the following subobjectives.

- Build a simplified functional model of an engine cylinder cooling jacket using ANSYS® Fluent® and validate it by comparing it with data available in the literature.

- Propose and analyze cylinder cooling jacket designs with modified topologies with the aim of enhancing their heat transfer properties. Enhancements will be based on the addition of adiabatic baffles and additional fluid outlets.

3. MATERIALS AND METHODS

3.1. HARDWARE AND SOFTWARE USED

A desktop computer equipped with a 4-core Intel i5 CPU running at 3.50 GHz and 8 GB of RAM running at 1600 MHz was used to run the simulations presented in this work.

The CFD simulations were performed using the Fluent® Fluid Flow software included in the 2020 R2 version of ANSYS® Academic. The ANSYS® academic software either using a free student license (as in this work) or a paid campus license presents an upper limit of 512000 computable elements to avoid any commercial usage at a reduced cost.

Geometry files were generated through Autodesk's AutoCAD® 2021 using a student license. AutoCAD® was chosen over ANSYS®-integrated CAD software due to previous knowledge from the author and due to a better recognition of geometry contact points by ANSYS®.

3.2. PRE-PROCESSING

3.2.1. Model design

Simulation geometrical models were designed to resemble the cooling jacket in the engine of the Honda CB125R from 2018, an engine formally identical to that on figure 1 of this work (see section 1.1.1.). The CB125R is a naked-style sports motorcycle featuring a liquid-cooled single-cylinder 125 cc gasoline engine that generates a maximum power output of 9.8 kW. Liquid cooling of said engine is achieved by forced circulation of a 50% $^{V}/_{V}$ mixture of ethylene glycol and water through a cooling jacket around the outer face of the cylinder wall [25]. This engine was chosen by the author due to ownership of a CB125R motorcycle.

The cylinder wall and cooling jacket thickness could not be obtained from the manufacturer for this or any similarly sized engines and were calculated based on literature data on larger engines by maintaining the same wall/jacket thickness to cylinder bore ratio [19]. By using this

approach, a 4.7 mm cylinder wall thickness was obtained which was rounded to 5 mm. A 5.3 mm thickness was obtained for the cooling jacket which was also rounded to 5 mm. The outer wall, which separates the cooling jacket from the environment was approximated to be half the thickness of the inner wall due to lower mechanical requirements (see figure 5). The aspect ratios obtained for the mentioned regions were comparable to what can be found on other references [26, 1].

Table 2. Engine specifications Honda's 2018 CB125R sports motorcycle [25].

Parameter	Value
Maximum power output	9.8 kW
Maximum torque output	10.0 N·m
Cylinder bore*	58.0 mm
Cylinder stroke*	47.2 mm
Engine building material	Cast aluminum
Cooling fluid	Ethylene glycol - water 50% $^{V}/_{V}$

(*) All of the stroke length and cylinder perimeter was considered available for heat transfer.

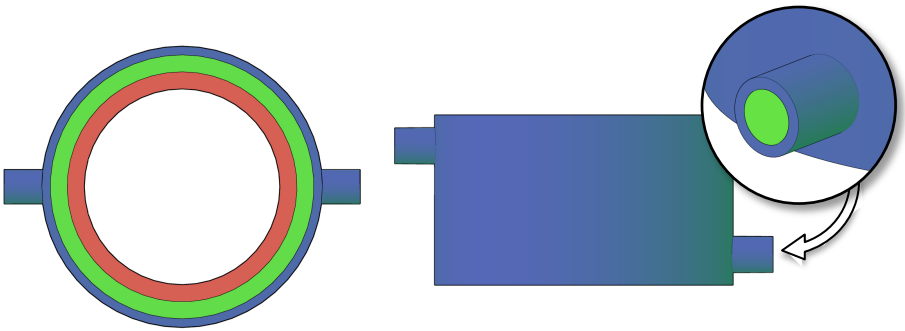

Figure 5. Top view (left), side view (right) and inlet detail view (top right) of the model. The diagram is drawn to scale and has been color-coded as follows: Inner wall Cooling fluid Outer wall / rubber tubing.

Inlet and outlet position and size were determined based on observation of the motorcycle and publicly accessible technical diagrams from an online parts store [27]. Both were determined to be using steel-reinforced rubber hoses with an outer diameter of 10.0 mm and a

thickness of 1.5 mm. The inlet and the outlet were determined to be at a small distance relative to the end of the stroke which was approximated to 3.5 mm. Their relative position was found to be nearly opposed with the inlet in the lower end of the stroke and the outlet on the upper end to take advantage of the thermosyphon effect and reduce pumping requirements (see figure 5).

The sharp turn around the inlet and outlet hose regions was later found to be problematic in terms of meshing and convergence. To address this, the model was further simplified. This new model did not include any length of cooling hoses nor did it include any solid walls: only the fluid was drawn and meshed. Since the system presented bilateral symmetry, only one half of the cooling jacket was studied. This helped to further decrease element size and improve convergence (see figure 6).

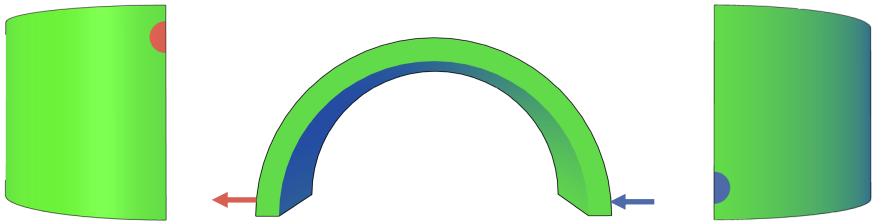

Figure 6. Outlet side view (left), top view (center) and inlet side view (right) for the further simplified model. Note that only one half of the fluid jacket was considered. The diagram is drawn to scale and its color coding is as follows: Outlet Cooling fluid Inlet.

Models with heat transfer enhancing devices were designed based on the same principles as the simplified model above. Baffles were initially designed as planar surfaces with no thickness which proved being problematic in terms of meshing. Consequently, baffles were finally designed as solids with a 1 mm thickness. Even with the inclusion of baffles, only the fluid was studied. This section shows one of the proposed prototypes for illustrative purposes only. Since the design of each prototype is based on previous prototypes and their simulation results, this and other designs can be found in the results section (see figure 7).

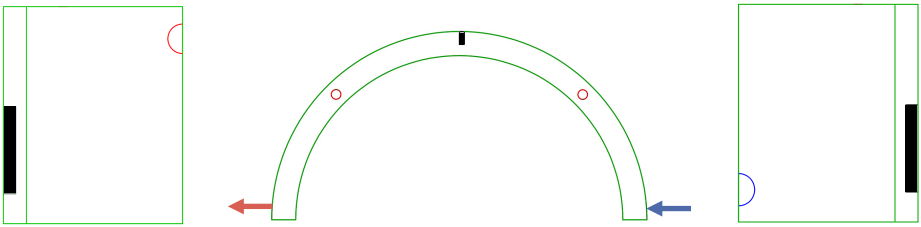

Figure 7. Outlet side view (left), top view (center) and inlet side view (right) of a model containing a baffle. Note that representation style has been changed to wireframe in order to make the baffle visible and that hidden lines are presented as a continuous line. The diagram is drawn to scale and is color coded as follows: Outlets Cooling fluid Inlet Baffle.

3.2.2. Meshing

The meshing of the geometrical models was done on the Meshing™ software included in the ANSYS® Workbench™ engineering suite. The meshing process was always started by creating named selections for all faces of interest such as inlets, outlets, walls, etc. By doing so, all downstream procedures become simpler because each part of the model can then be referred to it by its name instead of selecting it on the 3D geometry (which can be troublesome or, at least, slow for inner walls). Unless otherwise stated, mesh parameters were used on their respective default value.

The freestream fluid was meshed automatically by the software using the CFD default tetrahedral mesh. The element size was adjusted by the use of the "adaptive sizing" tool at its maximum resolution (7/7) with all other parameters set to their most sensitive value (see table 3 and figure 8, left). No automatic inflation was used in any simulation.

Table 3. Adaptive sizing parameters used for freestream fluid meshing.

Adaptive sizing parameter	Value
Resolution	7 out of 7
Mesh defeaturing	Yes
Defeature size*	Default
Transition	Slow
Span angle center	Fine

(*) Default defeature size is calculated by the software depending on the geometrical model.

Mesh quality was monitored using skewness and element quality (both magnitudes range from 0 to 1). In the CFD community, it is common practice to limit average skewness to 0.3 (maximum skewness should be kept under 0.95) and to avoid the presence of elements with orthogonal quality below 0.1 [28]. Skewness is defined as the difference between the shape of the cell and a prototypical cell of equivalent volume. Orthogonal quality is a related parameter based on the deviation of the angles between the element's faces or edges from their respective prototypical value [29]. To improve mesh quality and make convergence faster (or possible) the target skewness of the mesh was set to 0.3 with the smoothing option set to high.

To obtain an accurate solution, areas with great gradients of any property should be finely meshed [28]. The manual inflation tool was used on all models to increase the mesh density in the proximity of all walls (including inlets and outlets), where great momentum and/or temperature gradients are present (see figure 8).

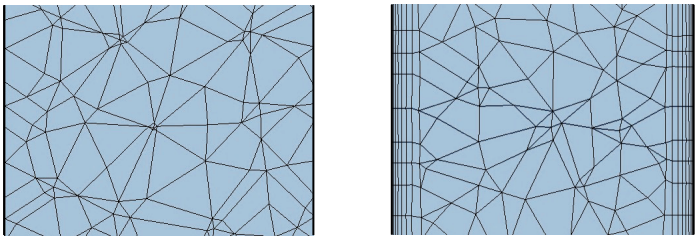

Figure 8. Cross section of a cooling jacket prototype showing the tetrahedral mesh of the freestream fluid (left) and the same cross section with the addition of the inflation layer (right).

The inflation region was defined based on the thickness of its first layer, with 6 to 10 layers depending on the number of elements available after the global automatic meshing was performed. The thickness of the first layer was iteratively adjusted so that the wall y^+ value did not exceed a value of 1 in any point of the system, a requirement of the turbulence model used in this work in order to attain adequate near-wall fluid treatment [21] (see section 1.2.2.2. for more information). The layer thickness growth rate was adjusted to obtain a smooth transition between the inflation region and the freestream fluid mesh. The inflation algorithm was set to "Post" (inflation layer being created after the tetrahedral mesh [28]) because it was found to work more robustly around corners and sharp turns in complex models than the "Pre" algorithm.

To avoid divergence-inducing mesh artifacts at their respective meeting areas, all inflation regions were identically defined (see table 4).

Table 4. Inflation parameters used for near-wall fluid meshing.

Inflation layer parameter	Value
Inflation option	First layer thickness
First layer Height	$5 \cdot 10^{-7}$ to $2 \cdot 10^{-5}$ m
Maximum layers	6 to 10
Growth rate	1.2 to 4
Inflation Algorithm	Post

In cooling jacket prototypes containing baffles, further refinement of the mesh around said flow modifiers was necessary to ensure an accurate description. The inflation tool creates a refined mesh in the direction normal to walls but does not affect the face mesh density. In addition to inflation around the baffle, the sizing tool was used to refine the mesh on its faces. The face sizing was based on an element size of 0.35 mm and its behavior was set to soft, so it did not override other local mesh characteristics such as the beforementioned inflation. In addition to the baffle faces, the sizing tool was also used to create a locally denser mesh in the fluid around it by the use of the "influence volume" option with an affected distance of 1.0 mm. When activated, this tool creates an extension of face mesh into the fluid that in conjunction with the inflation allowed for an accurate description of mesh (see table 5 and figure 9).

Table 5. Face sizing parameters used for mesh refinement around baffles.

Face sizing parameter	Value
Type	Element size
Element size	0.35 mm
Defeature size	Default *
Influence volume	Yes
Affected distance	1.0 mm
Behavior	Soft

(*) Default defeature size is calculated by the software depending on model characteristics such as element size.

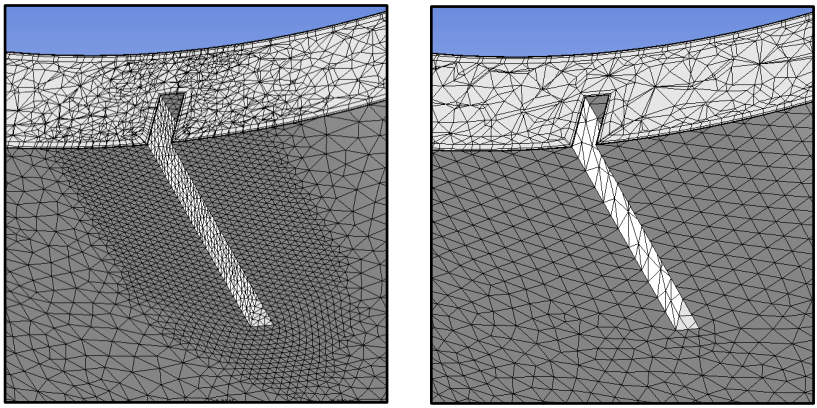

Figure 9. Meshing for a prototype containing a baffle with inflation on all faces of the model and face sizing with a volume of influence on the baffle faces (left) compared to the same model without face sizing (right). Note that without face sizing the mesh on the baffle faces is only a few elements across.

3.3. SIMULATION SETUP

The simulation setup is the first step that is done on the Fluent® software itself. During the setup, all the simulation parameters except for the geometry and the meshing must be defined. The double precision 3D solver option was selected on Fluent® startup as it is recommended by the ANSYS® Fluent® user's guide for meshes with a wide distribution in element size as the ones used in this work [30]. Before entering any values, the mesh quality was further improved by the use of the "Improve Mesh Quality" tool on Fluent®. The tool was set to improve the 10% worst quality cells (the maximum) in 4 iterations (the default value).

Any parameters not listed in this section can be assumed to be used on their default value.

3.3.1. General setup

Solver type and velocity formulation were set to their default value: "pressure-based" and "absolute" respectively. Since the simulation was on a steady-state system the time parameter was set to "steady". To account for buoyancy effects, gravity was activated with a gravitational acceleration of 9.8 m/s^2.

3.3.2. Transport and viscous models

The energy model was activated so that the software would solve the energy equation across the system.

An approximated Reynolds number based on the circulation of the fluid through a circular annulus with the dimensions of the system was calculated. Values ranged from 7 000 to 10 000 indicating that the circulation regime was turbulent or transition-turbulent. Note that since these calculations were done assuming a uniform temperature of 90ºC across all fluid the calculated Reynolds number could be underestimated.

Related work from Shingare et al. [19] and Magryta et al. [26] showed that the Realizable k-ε turbulence model with enhanced wall treatment provided accurate results for the flow through engine coolant galleries when compared to experimental data. This was also in agreement with the ANSYS® Fluent® theory guide which states that the Realizable k-ε model is applicable on industrial flow and heat transfer simulations with turbulent circulation where detailed treatment of the viscous layer is not required. By using the enhanced wall treatment with the first node at $y^+ \leq 1$ an accurate yet robust description of the near-wall flux can be attained (comparable to the use of turbulence models with rigorous wall treatment but without their computational needs [21]).

Model constants were all set to default values (see table 6) and the “buoyancy effects” option was also set to its default value: “only turbulence production”.

Table 6. Default values for the Realizable k-ε turbulence model.

k-ε realizable model parameter	Value
C2-epsilon	1.9
TKE Prandtl Number	1.0
TDR Prandtl Number	1.2
Energy Prandtl Number	0.85
Wall Prandtl Number	0.85

3.3.3. Materials

The cooling fluid specified by the manufacturer for the engine object of this work is a 50% by volume mixture of ethylene glycol (EG) and water (W) compliant with the ASTM D-3306

standard for corrosion inhibitors and stabilizer contents [31]. Temperature dependent properties were used for the description of the cooling fluid. Experimental data was obtained from the work of Å. Melinder [9] and was fitted to suitable expressions (table 7). Regression data and plots can be found on Appendix 1.

Table 7. 50% EG-W mixture's thermophysical properties versus temperature regressions.

Property	Adjusted equations	R^2
Density	ρ [kg/m^3] = $-1.1972 \cdot 10^{-3} \cdot T^2 - 4.8183 \cdot 10^{-1} \cdot T + 1.0890 \cdot 10^3$	0.9988
Specific heat	C_P [J/(kg·ºC)] = $3.0658 \cdot T + 3.4117 \cdot 10^3$	1.0000
Conductivity	k [W/(m·ºC)] = $-1.6277 \cdot 10^{-6} T^2 + 6.8664 \cdot 10^{-4} T + 3.5427 \cdot 10^{-1}$	0.9999
Viscosity	μ [kg/(m·s)] = $5.7480 \cdot 10^{-7} \cdot \exp(2.5647 \cdot 10^3 \cdot T^{-1})$	0.9891

Since solid materials were only considered in the early stages of this work, research was done using the Fluent®-included aluminum material with constant thermophysical properties (see table 8).

Table 8. Fluent®-included Aluminum solid properties.

Property	Value
Density [kg/m^3]	2719
Specific heat [J/(kg·ºC)]	871
Thermal conductivity [W/(m·ºC)]	202.4

3.3.4. Boundary conditions

3.3.4.1. Inlet

The inlet face on the model was set to a "mass flow inlet" boundary on the Fluent® setup. Turbulence intensity and turbulent viscosity ratio were set to 5% and 10 respectively because Magryta et al. [26] found that convergence was good on similar systems and Shingare et al. [19] found that results were accurate to reality. The direction of the flow at the inlet was set to be normal to the boundary.

Since no data was found on the mass flow rate (FR) for coolant in similarly sized engines a literature review was needed in order to adjust the coolant flowrate from larger engines. As in most of the literature, two scenarios were studied in this work: a high-load and high RPM situation (high coolant flow rate and a high heat load) and a part load mid RPM situation (lower coolant flow rate and heat load). Several flow rate candidates were found on the literature [19, 26, 32] and recalculated for the smaller displacement of the engine that object of this work based on cylinder volume. An approximated Reynolds number considering transverse flow through the circular corona of the cooling jacket ($A_{\perp} = 1{,}147 \cdot 10^{-3}$ m^2) was calculated for each case and a decision was made based on the criterion found on SCU's cooling design considerations guide [33]. Authors of said guide recommend using a turbulent coolant flow but to avoid Reynolds numbers exceeding 10 000 to avoid excessive pumping power requirements. Jack and Ojapah [32] place that limit on a speed of 1.8 m/s. Both requirements were fulfilled by the calculated flowrates from the work of Shingare et al. [19] (see table 9).

Temperature on the inlet was set to 90ºC, a value that the vast majority of authors agree on [19, 26, 32, 34] and is the automotive standard of today since it allows for optimal operation of the engine (good fuel vaporization, lowered oil viscosity...) yet retaining a safe temperature margin until phase change could occur. Large margins are needed since automotive engines encounter high variability scenarios such as high load spikes or transitory periods of compromised cooling as when coming to a stop with a heat-soaked engine.

Table 9. Engine coolant rates used in the simulations.

Reference	Scenario	FR_{REF} [kg/s]	FR_{CALC}* [kg/s]	**v** [m/s]	**Re** [-]
Shingare *et al*. [19] V_{CYL} = 1125 mL	Part load	4.5	0.50	0.44	6 500
	Full load	7,0	0.78	0.65	9 700

(*) Note that since models only include half of the cooling jacket, the flowrate used in the simulations was half of the FR_{CALC} value.

3.3.4.2. Outlet

The outlet face or faces were set as a "pressure outlet" with outcoming flow normal to the boundary. As with the inlet, turbulence intensity and turbulent viscosity ratio were set to 5% and 10 respectively. Pressure of the outlet was set to 2.0 bar relative pressure to ensure phase change prevention during normal operation. Pressurized systems with relative pressures

ranging from 0.3 to 2 bar are common in the automotive industry [10]. Since increasing coolant temperature reflects in enhanced thermal efficiency of the engine, nowadays it is increasingly common to find relative outlet pressures in excess of 1.5 bar [35].

3.3.4.3. Inner wall

The inner wall of the cooling jacket, also referred to as the cylinder wall, is the boundary that separates the engine's combustion chamber from its surroundings (including the engine coolant). This wall is the surface with the greatest cooling needs of the engine and, based on this premise, in this work it was considered the only point for heat entry to the engine coolant. No data was found on wall temperature for the engine object of this work nor for similar models. To define this boundary condition using experimental or available engine data, a wall temperature was calculated from experimental / available data with the help of ANSYS® Fluent® simulations.

Simulations were performed based on a heat flux density calculated combining experimental engine output work [25] or thermal power input with estimated thermal efficiency and power-to-coolant ratios extracted from the work of Howden and Singh at the US Department of Energy [36]. Again, partial engine load and full output scenarios were considered (see table 10). For the full load scenario, the thermal power consumed was calculated from the maximum engine output and its thermal efficiency and was then used to estimate the power to the coolant and wall heat density figures. For the part load scenario, thermal power used was extracted from experimental fuel consumption measurements when driving the motorcycle at 80 km/h in top gear on a leveled road. Measurements reported a fuel consumption 2.2 L / 100 km which was converted to a thermal power figure by considering that gasoline contains 44.4 MJ/kg and has a density of 800 kg/m^3 at 20 ºC [37].

Area-weighted wall temperature averages were extracted from the heat flux density simulations and were used to perform the simulations in this work. Temperature averages were 137 ºC for the part load scenario and 154 ºC for the full load scenarios. These temperatures fall within the range expected for a spark-ignited engine and is comparable to values found on CFD-based references [19, 26] or experimental data [38].

Simulations were run with temperature-based boundary conditions so that when heat transfer improvements were applied to the system, they would reflect in higher outlet

temperatures or higher wall heat flux density. If a heat flux density boundary was to be used, improvements in heat transfer would not make any effect since the amount of heat exchanged between the inner wall and the coolant would be always the same: the imposed boundary condition.

Table 10. Wall heat density data and intermediate results from its calculation.

Parameter	Part Load	Full Load
Work produced [kW]	3.25	9.8*
Thermal efficiency [(a)] [%]	20	30
Thermal power used [kW]	16.3*	31.7
Thermal power to coolant [(a)] [%]	15	15
Thermal power to coolant [kW]	2.44	4.76
Exchange Area [m^2]	$1.01 \cdot 10^{-2}$	$1.01 \cdot 10^{-2}$
Wall heat density [W/m^2]	$2.42 \cdot 10^5$	$4.72 \cdot 10^5$

(a) extracted from the work of Howden & Singh at the US Department of Energy (DOE).
(*) Input parameter for wall heat density calculation.

3.3.4.4. Outer wall

To take into account the amount of heat lost through the system's uninsulated external wall its temperature was set at 90 ºC as Merati et al. [39] found that the surface of the engine block for a stationary vehicle once its engine is off can be assumed to be around that temperature. Note that this temperature is only an approximation as real values depend not only on engine load but also on vehicle speed and the possibility of heat soak (heat from a past high load period affecting present engine temperatures). Although outer wall temperatures for a partially loaded engine surrounded by air circulating at high-speed, e.g., 80 km/h, could be significantly lower, the 90 ºC experimental value was considered valid for the achievement of the objectives in this work.

3.3.4.5. Other walls

Since engine oil and parts with temperatures similar to that of the coolant are behind the upper and lower walls (see section 1.1.1.), these were considered adiabatic ($q = 0\ W/m^2$).

Baffle walls were also set up as adiabatic so that the increase in wall surface did not cause an overestimation of the improvements in heat transfer derived from enhanced flow patterns (baffles were mostly located on the outer wall at a temperature of 90 ºC).

Walls representing symmetry planes were set to “Symmetry” type on the Fluent® setup.

3.3.5. Solution setup

3.3.5.1. Solution methods

A pressure-velocity coupled solver scheme was used to solve the model. Coupled solvers can take more time per iteration but are more robust and require fewer iterations for convergence than segregated solvers [30]. The pseudo-transient option, a form of implicit under-relaxation [21], was activated (it is the default option for steady-state single-phase flow cases).

Spatial discretization was set to second order for all variables as greater precision is recommended to obtain accurate results when the mesh is not aligned with the flow direction as in this work [30]. Using the same criterion, gradients were set to be calculated based on least squares, the most precise setting (see table 11).

Table 11. Spatial discretization settings summary.

Property	Discretization scheme
Gradient	Least Squares Cell Based
Pressure	Second Order
Momentum	Second Order Upwind
Turbulent Kinetic Energy	Second Order Upwind
Turbulent Dissipation Rate	Second Order Upwind
Energy	Second Order Upwind

3.3.5.2. Solution controls

The solution controls for the selected solver scheme consist of pseudo-transient explicit relaxation factors. These factors influence the impact that calculated values have on the current

iteration with 1 meaning full effect and a value close to 0 meaning no effect at all. Lowering the relaxation factors can often have beneficial effects on solution robustness and stability at the cost of slower convergence [21]. In this work all relaxation factors were set to their default value (see table 12).

Table 12. Pseudo transient explicit relaxation factors summary.

Property	Factor
Pressure	0.5
Momentum	0.5
Density	1
Body Forces	1
Turbulent Kinetic Energy	0.75
Turbulent Dissipation Rate	1
Energy	0.75

Convergence detection was based on the default scaled residuals values of $1 \cdot 10^{-3}$ for all magnitudes except for the energy scaled residual which has a default value of $1 \cdot 10^{-6}$. The outlet temperature and the inner wall to coolant average heat transfer coefficient were monitored (plotted in every iteration) during the calculation process to ensure that these (and indirectly other) variables were stabilized at the moment of convergence declaration.

3.3.5.3. Solution initialization

Solution was initialized using the standard initialization method based on all model zones. By doing so, the system calculated turbulence parameters and then an initial value was manually set for x, y and z velocities and temperature based on the experience gained in former simulations.

3.4. POST-PROCESSING

3.4.1. ANSYS® Fluent® Solution reports

The output of the simulations was first characterized and manipulated on the Fluent® Solution section using surface integral reports for the magnitudes susceptible of study. These

magnitudes included y^+, heat transfer coefficients, wall temperatures and inlet pressure (see table 13).

Table 13. Fluent® Solution reports summary.

Magnitude	Surface integral type
Wall y^+	Maximum, average and minimum across model.
Average heat transfer coefficient	Area-weighted average on the inner and outer walls.
Wall-adjacent fluid temperature*	Area average on an isosurface at 0.02 mm from inner wall.
Outlet temperature†	Mass-weighted average at the outlet/s
Inlet pressure	Area-weighted average on inlet face.

(*) Wall-adjacent fluid temperature will be acronymised as WAFT throughout this work.

(†) When multiple outlets were present, the mass-weighted average considered all outlets.

When calculating heat transfer coefficients (HTC) through CFD software caution should be applied as they are subjective and macroscopic measures that require the definition of a fluid bulk temperature. Different coefficients will be obtained if different bulk temperatures are used, so care must be taken to ensure that a valid and uniform criterion is used to make comparisons possible. The ANSYS® Fluent® CFD software calculates the heat transfer coefficient from the macroscopic equation that can be found on classical engineering books [40, 41]:

$$q = h\,(T_W - T) \;\rightarrow\; h = \frac{q}{T_W - T} \tag{10}$$

Where q is the heat flux density through the wall, T_W is the temperature of the wall and T is the bulk temperature for the fluid. In this work, the bulk temperature was calculated as the arithmetical average between the inlet and outlet temperatures of the different models as it is common practice when performing classical engineering heat transfer coefficient calculations on heat exchangers [40].

Great caution must be applied when calculating heat transfer coefficients using the ANSYS® Fluent® software as the bulk temperature is defined to be equal to the reference temperature which is 15 ºC by default. If inadvertently left on its default value, the heat transfer coefficient values obtained will not match the classical definition (see equation 10) nor will be valid for a comparison among different systems.

3.4.2. ANSYS® CFD-Post Reports

ANSYS®-integrated CFD-Post software was used to generate contours and plots for wall temperature and fluid trajectories (streamlines). The range of the variables on all representations was manually limited to enhance the results clarity and keep them comparable (table 14). Note that, unless otherwise stated, the same view is used for every representation in this work: a view from the outside of the cooling jacket with the main inlet on the bottom left part of the picture and the main outlet on its upper right side.

Table 14. CFD-Post solution representations summary.

Representation	Characteristics
WAFT contour	Temperature on an isosurface at 0.02 mm* from inner wall Display range limited to [90 ºC, 140 ºC]. 50 contours. Fluent® rainbow color scheme with no shade.
Hotspot highlight contour	WAFT on an isoclip with temperatures higher than average and higher than average + 5%. Display range limited to [90 ºC, 140 ºC]. 50 contours. Fluent® rainbow color scheme with no shade.
Fluid trajectory streamline (3D trajectories)	Velocity display range limited to [0 m/s, 5 m/s]. 50 streamlines starting from inlet face. Fluent® rainbow or inverted greyscale color scheme.
Velocity contour	Velocity on an isosurface at 0.02 mm* from inner wall. Velocity display range limited to [0 m/s, 2 m/s]. Fluent® rainbow color scheme with no shade.

(*) The 0.02 mm value was chosen for the first and simplest model as it corresponded to an average $y^+ = 30$ (the limit for the wall affected region of a turbulent flow, see section 1.2.2.) which clearly showed the effects of flow patterns on wall adjacent temperatures and velocities (as opposed using to the first node on the wall, which always showed temperatures close to the wall temperature and velocities close to 0 m/s). This value was used for all systems to keep the results comparable.

4. SIMULATION RESULTS AND DISCUSSION

In the following section, results from the simulations of systems with smooth cooling jackets (section 4.1) and their enhanced counterparts (section 4.2) will be presented and analysed.

4.1. SIMULATIONS ON SMOOTH COOLING JACKETS

Simulations for part load and full load conditions were run using the models and conditions described in section 3. Their results will be presented and analysed in the following subsections.

4.1.1. Part load scenario

The simulation results for the part load case of the smooth cooling jacket will be discussed in the following sections (T_{WALL} = 137 ºC and FR = 0.50 kg/s).

4.1.1.1. Mesh validation

The mesh independency of the results was tested by running simulations with coarser and finer meshes. The mesh was proportionally scaled, e.g., a coarser tetrahedral freestream fluid mesh was accompanied by less inflation layers, etc. The first element height for the inflation layer was kept constant at $5 \cdot 10^{-6}$ m in order to keep wall treatment consistent.

The outlet temperature was used as mesh diagnostic parameter due to its relevance in this work (see figure 10). Given the limitations of the academic software in terms of maximum computable elements, the results in the higher element region were considered mesh independent and valid for a semiquantitative analysis.

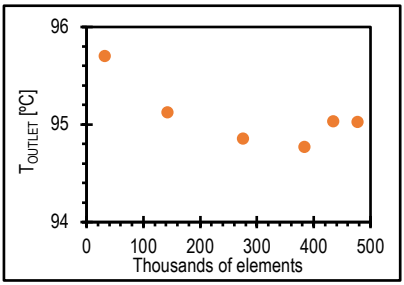

Figure 10. Mesh validation in terms of T_{OUT} (mass-average outlet temperature) for the part load scenario. Results were considered mesh independent and valid for a semiquantitative analysis.

4.1.1.2. Results

The wall-adjacent fluid temperature (WAFT, see section 3.4.1 for its definition) contour for the part load scenario shows a large hotspot on the top part of the cooling jacket (see figure 11). Since the boundary condition for the inner wall is based on a fixed temperature, greater WAFTs can only be caused by deficient (slower) coolant flow.

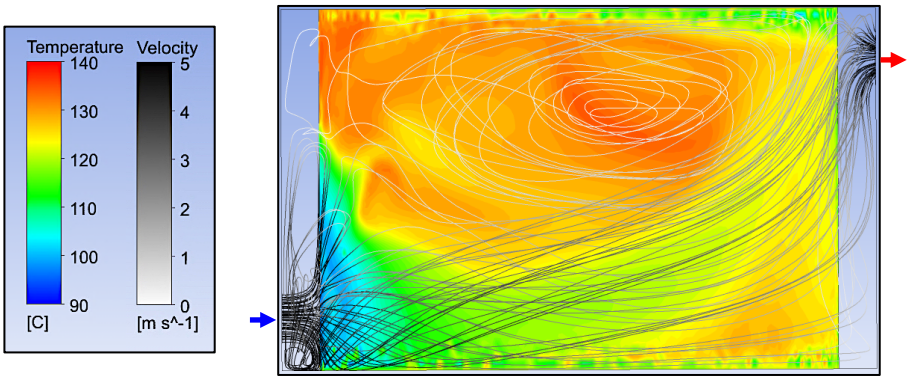

Figure 11. WAFT contour and fluid trajectory streamline combined representation showing a strong correlation between the coolant flow patterns and temperature for the partial load scenario. As for all the representations in this work, the inlet is placed on the bottom left and the outlet on the top right.

When the fluid trajectory is analyzed, a fluid short-circuit running from the intake to the outlet can be observed. This can be attributed to the topology of the simple model used in this work, which does not include any flow modifying devices nor any additional outlets to help direct the flow to otherwise dead or stagnated flow areas. Wall temperature and coolant flow characteristics show a strong correlation, with areas of stagnated flow presenting higher temperatures due to fluid heat up in dead zones. This phenomenon is especially pronounced in the area above the beforementioned short-circuit, where a large slowly revolving dead zone is present causing a large hotspot (see figure 11).

The WAFT was further characterized by computation of the relative area with a temperature higher than the area-weighted average, an indication of temperature uniformity and hotspot presence. The average wall-adjacent fluid temperature obtained was 122.5 ºC, with 64% of the area showing a temperature greater than average (figure 12, left) and a 26% exceeding average temperature + 5% (figure 12, right).

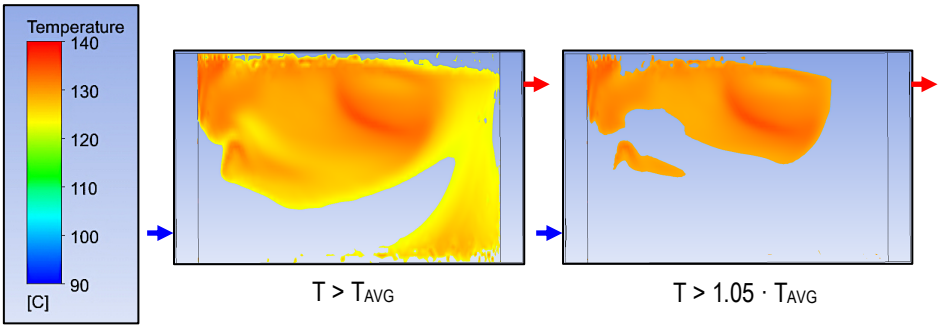

Figure 12. Wall adjacent fluid areas with temperature higher than average (left) and higher than average + 5% (right).

The mass-weighted outlet temperature obtained was 95.6 ºC, representing an increase from inlet temperature of 5.6 ºC. Its value is in agreement with experimental data available on the literature such as in the work of Magryta et al. [26], Burke et al. [42] or Haury and Volrkering [43] and is a first indication that boundary conditions and simulation models were chosen appropriately for a realistic description of the system.

The area-averaged heat transfer coefficients obtained in this simulation were 10700 and 13600 W/(m^2·ºC) from the inner and outer wall to the coolant, respectively. Both values are within the range expected for forced convection of a water-based liquid [41] and in agreement with experimental data on ICE convective cooling from the work of Robinson et al. [44]. The difference between the outer and inner wall coefficients cannot be attributed to the viscosity difference caused by temperature around said boundaries as the temperature is greater in the proximity of the inner wall which should cause a higher heat transfer coefficient. The difference could be caused by the velocity difference in proximity of the inner and outer walls. In the models presented in this section, the design of the inlet and the simplicity of the cooling jacket create a fluid dispersion towards the outer wall, which causes a velocity difference between the inner and outer walls. The higher speeds present in proximity of the outer wall could cause an increased turbulence intensity which in turn could be inducing a higher average heat transfer coefficient on the outer wall [40] (see figure 13).

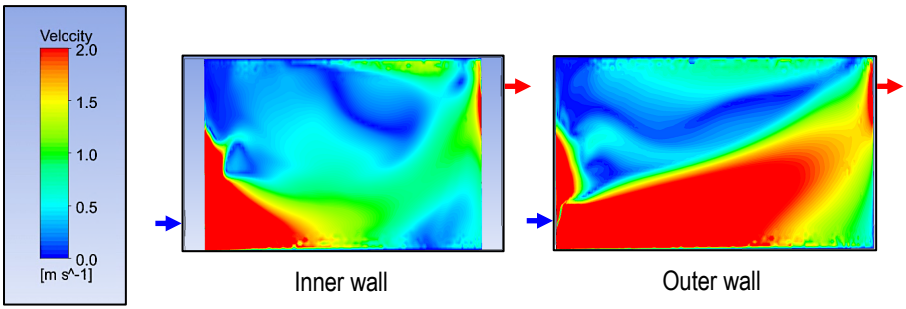

Figure 13. Wall-adjacent velocity on the inner wall surface (left) and outer wall (right). The greater heat transfer coefficient on the outer wall could be caused by a higher turbulence intensity (better mixing) caused by higher speed in proximity of this wall.

The pressure drop across the cooling jacket provided by Fluent® was 1.7 bar. No data was found in the literature for similar systems and since it is a magnitude strongly (and complexly) related to the topology of the system its extrapolation from the literature was not considered as a valid approach. As all other analyzed variables are in agreement with the data that can be found on the literature, this 1.7 bar value will be considered valid and taken as the baseline for the rest of the simulations.

4.1.2. Full load scenario

The simulation results for the full output case with a smooth cooling jacket will presented and analyzed in the following section (T_{WALL} = 154 ºC and FR = 0.78 kg/s).

4.1.2.1. Mesh validation

As in the previous section, the mesh for the full load scenario simulation was validated by running simulations at proportionally coarser and finer meshes and observing the same diagnostic parameter. The first element height for the inflation layer was kept constant at $1 \cdot 10^{-6}$ m to keep wall treatment consistent across all tested meshes.

Again, even though values were not completely mesh independent, considering the academic software limitations they were considered sufficiently stable to perform a semiquantitative analysis as their value was always in the same order of magnitude, especially in the higher element number region (see figure 14).

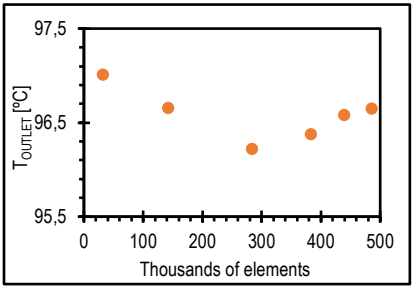

Figure 14. Mesh validation in terms of T_{OUT} (mass-average outlet temperature) for the full load scenario. Results were considered sufficiently mesh independent to perform a semiquantitative analysis.

4.1.2.2. Results

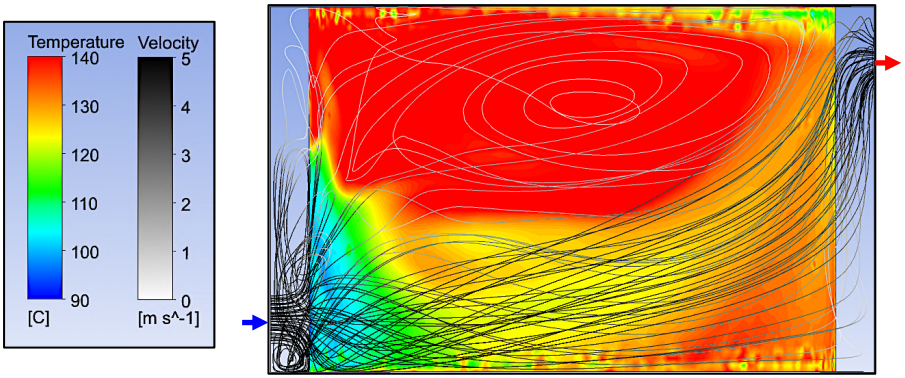

Figure 15. WAFT and fluid trajectory combined representation for the full output scenario showing a hotspot in the upper left section of the cooling jacket that could be caused by deficient flow in this area. A strong correlation is found between the flow pattern and the WAFT values.

As for the partial load case, the WAFT contour presents a large hotspot in the upper left part of the cooling jacket. Since the heat load is now higher, the wall adjacent fluid shows a globally higher temperature (see figure 15). Note that as the temperature range for the contours is fixed to keep the results comparable, the beforementioned hotspot may seem mistakenly larger than in the previous case. When the temperature range of the contour is readjusted (as in figures 16 left and right) the main hotspot (and even secondary ones) shows the same morphology and extension than for the lower heat load scenario.

As with the previous case, flow characteristics and WAFT show a strong correlation, with dead areas of the cooling jacket presenting the highest temperatures while areas of rapid flow present the lowest (see figure 15). Flow characteristics show very little difference from the part load scenario, with a large and slowly revolving vortex in the top left part causing the main hotspot and a very clear short-circuit running from the inlet to the outlet, decreasing the overall cooling capacity of the jacket. As stated in the previous section, these two flow properties could be caused by the simplistic design of this cooling jacket.

To further characterize WAFT and hotspot presence, areas with temperatures higher than average were represented and their relative extension was calculated. The area-weighted average for WAFTs was computed at 129.8 ºC with 56% of area with a temperature above average (figure 16, left) and 33% exceeding average + 5% (figure 16 right). This further characterization confirms that the hotspot morphology and extension is similar to the lower heat load case with the only difference present being its temperature, higher for this higher heat load scenario.

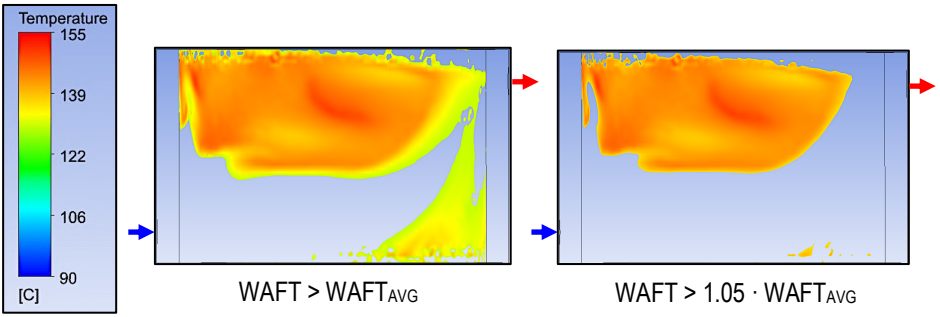

Figure 16. Wall adjacent fluid areas with temperatures higher than average (left) and higher than average + 5% (right). Hotspot morphology and extension is similar to the lower heat load case. Note that in order to gain display range, the upper temperature bound has been increased to 155 ºC.

Concerning temperature, for this high engine load scenario there are regions with WAFTs exceeding the coolant's bubble temperature at the 2.0 bar pressure used (see figure A1.5 in the appendix 1 for more information). It must be taken into account that the relative pressure in most of the cooling jacket will be greater than 2.0 bar, with a value on the inlet of 5.8 bar. Since only small regions close to the outlet could problematic it seems reasonable to state that boiling could be eliminated by improving the flow characteristics. Although it is not uncommon to find

nucleate boiling in some areas of the wall-adjacent fluid in engines performing at their full output, it is still a phenomenon that should be avoided to prevent wall fouling and coolant degradation [45, 46].

The outlet temperature provided by the simulator was 96.7 ºC. Its value is in the same range as for the part load scenario which further validates the boundary conditions used in this work and shows that the increase in heat load was compensated by the use of an adequately higher coolant flow rate.

Heat transfer coefficients obtained were 15000 and 21300 W/(m^2·ºC) from the inner and outer wall to coolant, respectively. These values are greater than for the part load scenario which can be attributed to the increased turbulence that comes with the circulation at a higher flow rate. Since the topology of the model is identical to that of the previous case, the difference between the inner and outer wall could also be attributed to a higher circulation speed on the proximity of outer wall as a consequence of the design of the cooling jacket. The heat transfer coefficients obtained are still within the expected range for forced convection of aqueous liquids [41] and are in agreement with experimental data from the work of Robinson et al. [44].

The pressure drop across the cooling jacket provided by Fluent® was 3.8 bar. This represents a 2.1 increase when compared to the part load scenario which can be attributed to the increase in the flowrate from the previous situation (0.5 versus 0.78 kg/s).

Table 15. Summary on inputs and outputs for the simulations on smooth cylinder cooling jackets.

Property	Part load value	Full load value
Wall temperature [ºC]	137	158
Mass flow rate [kg/s]*	0.50	0.78
T_{OUTLET} [ºC]	95.6	96.8
Area with T > T_{AVG} (+5%) [%]	64 (26)	57 (33)
$h_{IN,AVG}$ [W/(m^2·ºC)]	10700	15000
P_{LOSS} [bar]	1.7	3.8

(*) The mass flow rate for the modelled half jacket was half of this value.

4.2. SIMULATIONS ON ENHANCED COOLING JACKETS

As previously stated, the presence of hotspots on the cylinder wall is a phenomenon that must be avoided as they create thermal stresses that reduce the life expectancy of the materials in an engine. In this section, the results on simulations for cooling jackets with topology changes will be presented. The topology changes in the jacket cooling designs were oriented to increasing and, especially, homogenizing the heat transfer from the inner wall of the cooling jacket to avoid the presence of hotspots.

Due to its significance in terms of engine relative operational time, heat transfer enhancements were studied only for cooling jackets under partial engine load conditions. Results from this section will be compared to the ones presented for the smooth cooling jacket operating at a partial heat load which will be considered the baseline. Since similar results were obtained for the partial and full load scenarios in previous sections, it seems reasonable to state that the modifications that will be presented in this section could have had similar effects on the higher heat-load case.

4.2.1. Models

Several geometrical models of modified cooling jackets were developed and studied with the objective of improving the heat transfer capabilities of the simplified cooling jacket reviewed in previous sections (see section 4.1.).

Models were developed iteratively by trial and error. The aim of the improvements proposed was to disrupt the short-circuit between the inlet and the outlet found in the simpler model by redirecting the flow to areas where cooling was deficient. To achieve this, baffles were placed in different positions on the outer wall and additional outlets were positioned on the top part of the cooling jacket, where a dead zone was present in the simpler model (figure 17. See appendix 2 for other views).

Thanks to the quick modifications that the CFD simulations allow, a total of 7 prototypes with potential enhancements were tested. However, only 3 were considered valid as the rest did either not cause significative improvements or caused an improvement but a great deterioration on other areas. The models and simulation results for the discarded candidates can be found on appendix 3. Final candidates were named using acronyms related to their topology (see table 16).

Table 16. Prototype nomenclature and description.

Acronym	Description
O	Original design
VB	Vertical baffle
VBAO	Vertical baffle and additional outlets
AO	Additional outlets only

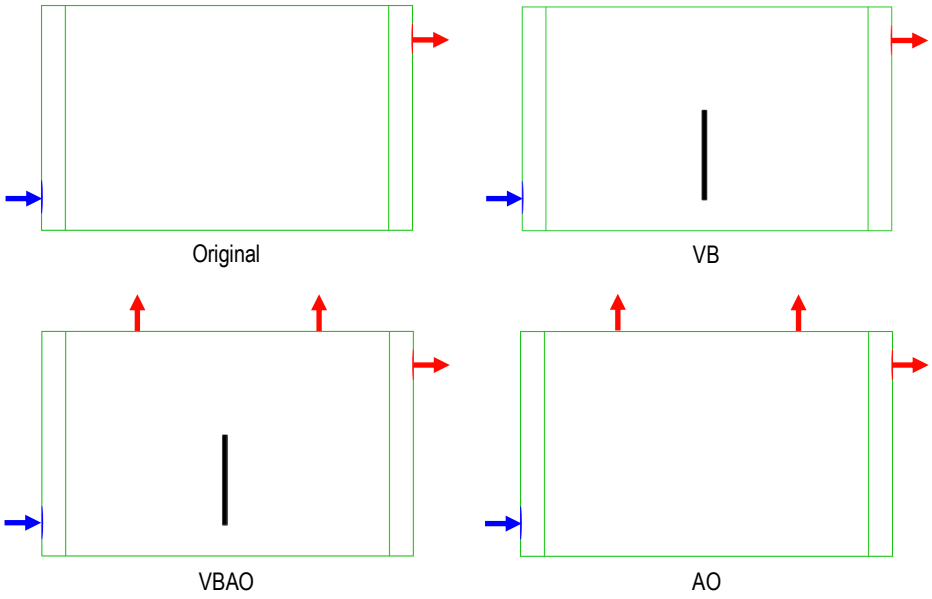

Figure 17. Proposed cooling jacket designs with modified topologies. Baffles present are placed on the outer wall. The original model is shown for comparison. The diagram is drawn to scale and is color coded as follows: Inlet Outlet Cooling Fluid Baffle.

4.2.2. Mesh validation

The mesh for the systems with topology changes was validated through the same procedure used on the original design: simulations were run on proportionally coarser and finer meshes while keeping the height of the cells in contact with the walls constant. The fluid outlet temperature was again used as the mesh diagnostic parameter due to its relationship with the heat transfer on the system.

Given the limitations of the academic version of ANSYS® Fluent® used, the results were only considered to be mesh independent enough to perform a semiquantitative analysis (see figure 18).

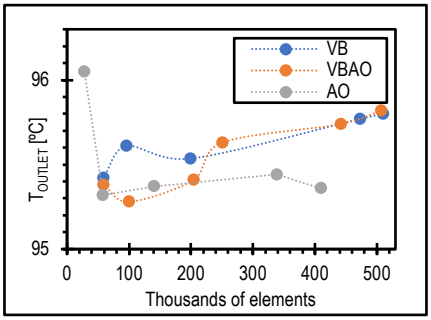

Figure 18. Mesh validation in terms of T_{OUT} (mass-average outlet temperature) for the modified topology cooling jackets. The results were considered sufficiently stable for a semiquantitative analysis. The data points have been joined with a dotted line to allow for an easier appreciation of the data trends.

4.2.3. Results

When the combined WAFT / fluid trajectory representations are analyzed for the cooling jacket designs equipped with a baffle (VB and VBAO models) a strong decrease of the WAFT values in proximity of the baffle can be appreciated (figure 19). As in previous models, WAFT values and flow patterns show a strong correlation, with areas of lower velocity showing higher temperature due to fluid heat up in these regions. The decrease in WAFT in the proximity of the baffle could be attributed to the fluid being deflected towards the inner wall due to the presence of said device. The addition of supplementary outlets in the top section of the VB prototype helped to slightly decrease the WAFT by enhancing the fluid flow in this area, where a large hotspot was present in the original models presented in this work. The addition of a single baffle, however, caused an increase in the WAFT values in the areas from which the flow was deflected. Since the area of influence of the baffle shows a sharp decrease in the WAFT, it seems reasonable to state that in a more complex design with multiple baffles of the same nature as the one used in this work it would be possible to attain a uniform distribution of WAFT.

When the same representation is analyzed for the model equipped with only additional outlets, a slight decrease in WAFT values in the top left part, where there was a large hotspot present in the original models, can be observed. Since there is a strong correlation in flow characteristics and WAFT, this decrease in temperature could be attributed to the increase in

the fluid flow velocities in this area, where the slowly revolving vortex present in the original model has been partially destroyed by the presence of the additional outlets (see figure 19).

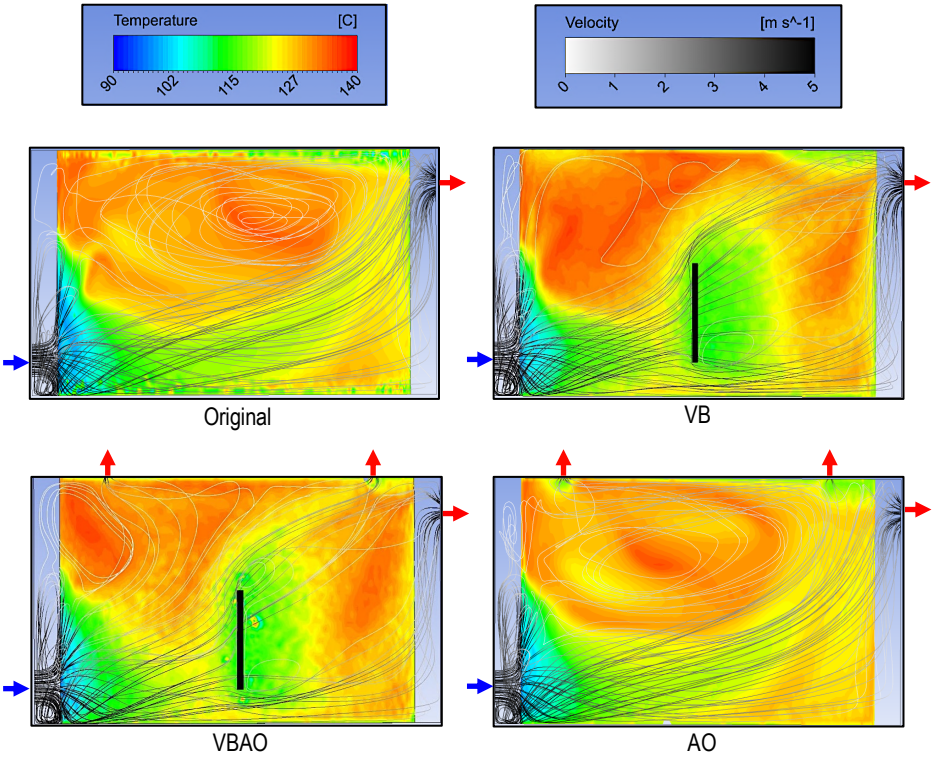

Figure 19. WAFT contour and fluid trajectory combined representation for the modified systems. The area around the baffles presents WAFT values lower than their environment and the additional outlets help to reduce the temperature on the top section of the jacket. The original design is shown for comparison.

As in previous sections, the presence and magnitude of the hotspots in the wall adjacent fluid was characterized in terms of the relative wall adjacent surface with a temperature higher than the average WAFT and also higher than the average WAFT + 5%. The models containing baffles in their topology (VB and VBAO) show significant differences in the hotspot morphology when compared to the original design, with the areas under the influence of the baffle presenting temperatures lower than the area-average for each system while some areas out the

influence of the baffle, notably the top left section of the cooling jacket, present a temperature higher than the baseline (see figure 20 and table 17). As previously stated, this could be attributed to the deflection of the flow towards the inner wall by the baffle which allows for better cooling of its areas of influence while depriving other areas of sufficient flux. As it could already be inferred from the WAFT contours, the addition of outlets in the top part of the cooling jacket further helped to reduce the hotspot presence on this top section, especially the presence of higher temperature hotspots (see figure 20 and table 17). These findings further support the statement that was previously made: it seems possible to completely homogenize the WAFT through the use multiple baffles on the outer wall.

The system equipped with only additional outlets (AO) as topology changes did also represent an improvement from the original design in terms of temperature uniformity, presenting a significantly lower area with a WAFT greater than average + 5%. This could be attributed to the enhanced flow characteristics in the upper section of the cooling jacket due to the presence of said outlets (see figure 20 and table 17).

Table 17. Summary of outlet temperatures and relative areas at a temperature higher than average for the prototypes with the proposed topology changes.

Design	$WAFT_{AVG}$ [ºC]	T_{OUTLET} [ºC]	A (A')* [%]
O	122.5	95.6	64 (26)
VB	123.6	95.8	59 (25)
VBAO	123.6	95.8	61 (19)
AO	123.3	95.4	69 (15)

(*) A: area with a WAFT higher than the WAFT average.
A': area with a WAFT higher than the waft average + 5%.

The outlet temperatures obtained for the cooling jackets with topology changes were not significantly different from the baseline value (see table 17). This could be attributed to the fact that for the tested prototypes, an improvement in heat transfer (diagnosed through lower WAFT) in some areas, which should have caused an increase in outlet temperature, was accompanied by a worsening in heat transfer in other areas due to flow deflection. This theory is further supported by the similarity among the WAFT average values for all tested prototypes, including the original design (see table 17).

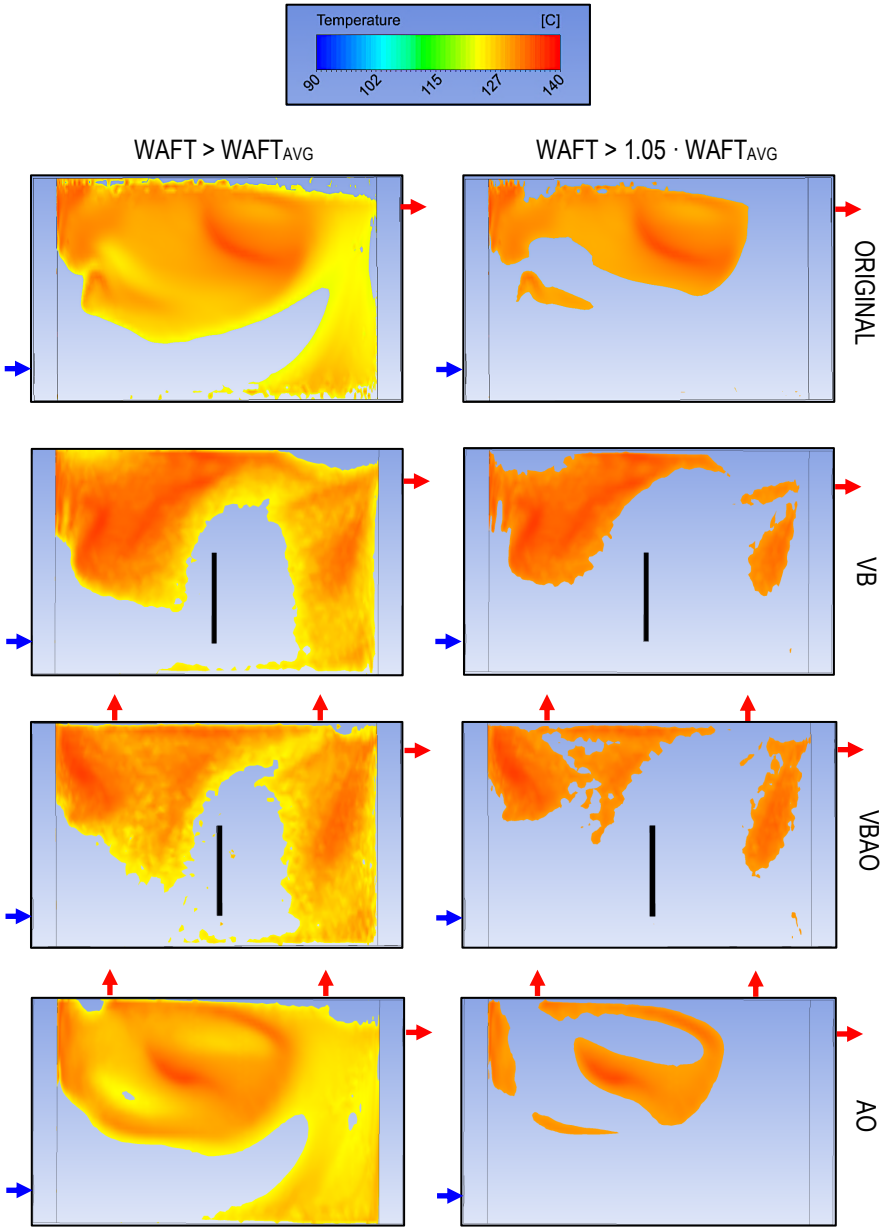

Figure 20. Hotspot characterization for the prototypes with topology modifications expressed as area at a temperature higher than average or higher than average + 5%. The original model is also shown for comparison.

All the heat transfer coefficients obtained for the prototypes with modified topologies were around 10 000 W/(m^2·ºC) (see table 18). Their values are therefore still in agreement with the range expected for forced convection of a water-based liquid [41] and with experimental data on ICE convective cooling from the work of Robinson et al. [44]. Heat transfer coefficients for the inner and outer walls are now closer in value than for the original model, which can be attributed to the higher degree of mixing due to the presence of the topology modifications.

For the designs containing baffles, as opposed to the original model, the heat transfer coefficient is now greater for the inner wall than for the outer wall. This could be partly attributed to the increased viscosity in the outer and cooler wall but since for the original model great velocity differences were found between the fluid in the proximity of the inner and outer walls, further investigation was performed in that direction. If a wall adjacent velocity analysis is performed for the prototypes containing baffles, it is found that the presence of said devices, as previously stated, causes a deflection of the fluid flow towards the inner wall increasing the mean velocity in the proximity of this surface while deteriorating the flow in proximity of the outer wall (see figure 21). As previously stated in this work, this lower velocity around the outer wall could be the cause of a less turbulent flow providing less mixing of flow therefore a lower heat transfer coefficient [40]. The absolute value for the inner wall average heat transfer coefficient however, remained unchanged from the baseline value, which could be a consequence of the flow characteristics, and thus heat transfer coefficient, which were improved in certain areas of the inner wall (such as the area of influence for the baffle) and deteriorated on others, compensating its effects. This theory is further supported by the conclusions extracted from the WAFT contours analysis.

Table 18. Average heat transfer coefficients for the models with topology changes. The changes in their relative magnitude have been attributed the velocity profile changes caused by the topology modifications.

Design	h_{IN} [W/(m^2·ºC)]	h_{OUT} [W/(m^2·ºC)]
O	10 700	13 600
VB	10 700	10 200
VBAO	10 600	9 200
AO	10 000	11 300

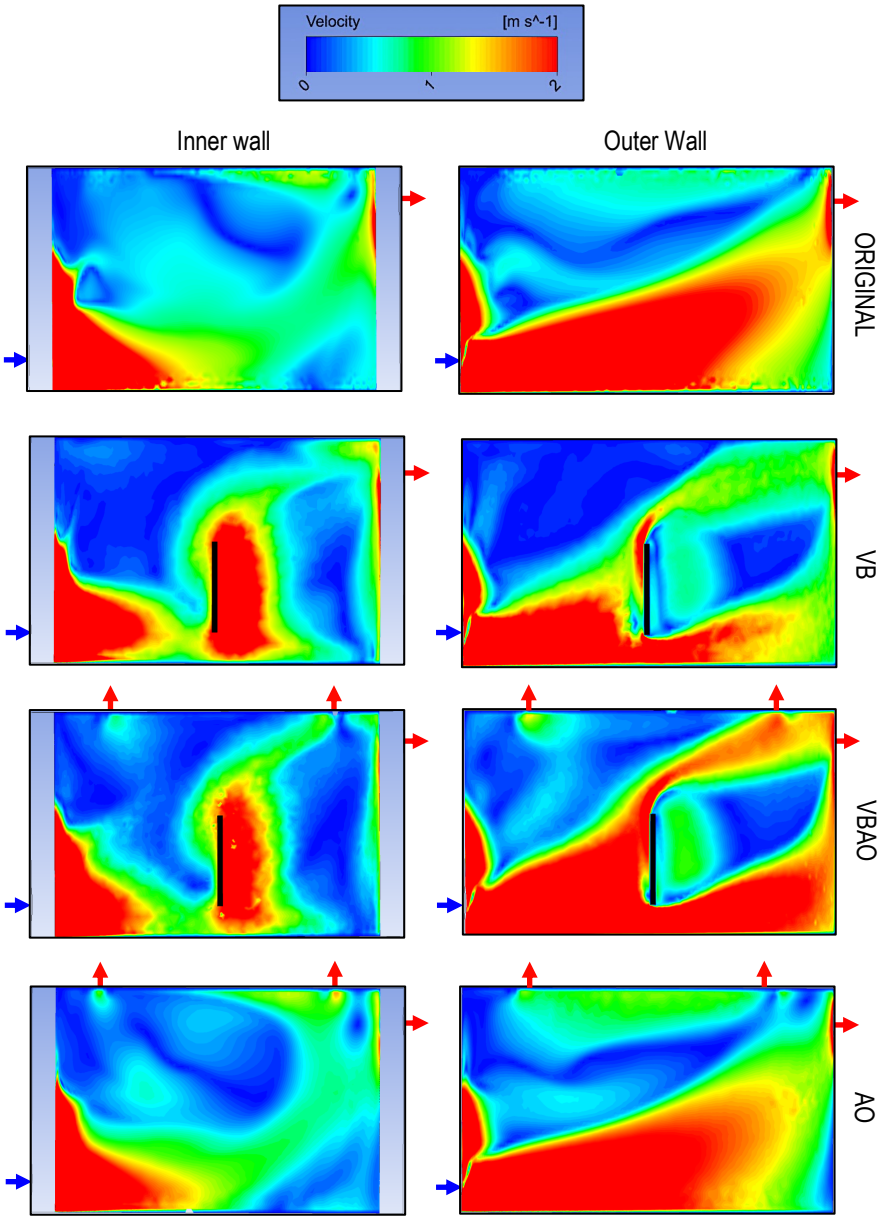

Figure 21. Velocity in proximity of the inner and outer walls for the systems with modified topologies. In models with baffles, a higher heat transfer coefficient for the inner than for the outer wall can be attributed to a flow deflection due to the presence of the baffle. The original design is shown for comparison.

The heat transfer coefficient values for the system with only additional outlets as topology modifications, presented a slight decrease for the inner wall heat transfer coefficient and a sharp decrease for the outer wall when compared to baseline. The decrease of both coefficients can be attributed to a more uniform but slower velocity distribution in the proximity of the walls which could be caused by the presence of the additional outlets (see figure 21). Additional outlets could be allowing for new fluid trajectories which in turn would cause a decrease in the velocity of formerly flow intensive areas (such as the main short circuit present in the original model). Although the velocity distribution resulting from the addition of supplementary outlets may be detrimental in terms of heat transfer coefficient average values, it still offers noticeable improvements in terms of WAFT uniformity (see figure 20).

Table 19. Summary of the outputs for the simulations on the cooling jackets with topology changes. The original design (O) is included for comparison.

Design	$WAFT_{AVG}$ [ºC]	A (A')* [%]	T_{OUTLET} [ºC]	h_{IN} [W/(m²·ºC)]	h_{OUT} [W/(m²·ºC)]	ΔP [bar]
O	122.5	64 (26)	95.6	10 700	13 600	1.7
VB	123.6	59 (25)	95.8	10 700	10 200	1.7
VBAO	123.6	61 (19)	95.8	10 600	9 200	1.3
AO	123.3	69 (15)	95.4	10 000	11 300	1.3

(*) A: area with a WAFT higher than the WAFT average.
A': area with a WAFT higher than the waft average + 5%.

The pressure drop for the system with a baffle as the only topology change (VB) was found to be identical to the baseline value of 1.7 bar. The lack of differences could be attributed to the small cross-sectional area of the baffle used and the fact that it did not occupy whole width of the cooling jacket, a characteristic chosen so that it would not cause hotspots in the inner wall due to flow a restriction. Systems with additional outlets either with or without baffles, presented a notable decrease in the pressure drop when compared to the baseline (see table 19). This could be attributed to the additional outlets creating new flow paths (more parallel paths available for the same flow rate may translate into less pressure drop) and due to the fact that these new paths are shorter than the ones that were previously available which went from the main inlet to the main outlet. The presence of more flow paths can also be attributed to cause a

lower average speed in each of the paths (see previous paragraph) causing lower friction losses and further lowering the pressure drop of the cooling jacket. Since in an internal combustion engine the cooling fluid is pumped by a centrifugal pump consuming power from the engine, lower pumping requirements could translate in a lower fuel consumption and more power available to move the vehicle (i.e., less parasitic loads).

5. CONCLUSIONS

The main objective of this work was to suggest topology changes in the cooling jacket of a single cylinder internal combustion engine to enhance its heat transfer characteristics using computational fluid dynamics simulations.

The author gained sufficient skill at using ANSYS® Fluent® academic CFD software which proved being adequate for the simulation of the cooling jacket in an internal combustion engine as the quality of the results suggests.

A simplified model of the cooling jacket in an internal combustion engine was successfully simulated using the academic version of ANSYS® Fluent® making use of the Realizable k-ε turbulence model and a mesh based on automatic sizing for the bulk of the and inflation and face sizing for areas with great gradients. The output parameters obtained were comparable to values from simulations or experimental data available in the literature and were used as the baseline for the improvements later introduced.

Topology changes in the form of a single baffle and additional outlets were introduced in the models with positive effects on the heat transfer characteristics. The combination of additional outlets and a baffle located on the outer wall of the cooling jacket provided the most promising results. The wall-adjacent fluid showed a sharp decrease in temperature in the area of influence of the baffle and a moderate uniformization in the temperature was found in the proximity of the additional outlets. The average heat transfer coefficients and outlet temperatures did not show remarkable differences from the baseline value. The pressure drop of the cooling jacket was not increased by the presence of the baffle used when compared to baseline. In fact, the beforementioned combination of topology changes considerably lowered the pressure drop of the cooling jacket with respect to baseline. The reduction in pressure losses was attributed to the inclusion of additional outlets.

6. FUTURE WORK

Since promising results were obtained in this brief preliminary research about the inclusion of baffles in the cooling jacket of an internal combustion engine, the author considers that further research could be done in this area. The following ideas had to be excluded from this work due to time constraints but may be developed in future work:

- Experimenting with simulations containing multiple vertical baffles located on the outer wall of the cooling jacket as well as additional outlets. Since in this work promising results for the temperature of the fluid adjacent to the inner wall in the area of influence of the baffle were found, it seems reasonable to state that this characteristic could be extended to the majority of the cooling jacket by the addition of multiple baffles.

- Experimenting with the topology of the inlet and the outlets, especially the secondary ones. Since the inlet topology used in this work caused the deflection of the flow towards the outer wall, sophistications such as an angled inlet could be investigated in future work. Regarding the additional outlets, since their effect in the results of this work was modest, more research could be performed in order to make them have a more significant impact on the temperature distribution in the proximity of the inner wall (use of larger outlets, non-circular geometries, etc.).

- Since it was found that on ANSYS® Fluent® the definition of the bulk temperature (involved in the calculation of the heat transfer coefficient) is user dependent it would be useful to develop a code (a Fluent® script) that would automatically calculate and change the bulk temperature value to its classical engineering definition once the calculation process was complete.

- And lastly, it would be interesting to further validate the results obtained in this work by performing experimental measurements on a single-cylinder liquid cooled engine of the same characteristics as the one modelled in this project or, at least, by running the simulations on a non-academic version of ANSYS® Fluent® using a denser mesh.

REFERENCES AND NOTES

[1] J. B. Heywood, Internal Combustion Engine Fundamentals, New York (New York): McGraw-Hill, Inc., 1988.

[2] Y. A. Çengel and M. A. Boles, Thermodynamics: An Engineering Aproach. 5th Edition, New York (New York): McGraw-Hill Science, 2004.

[3] A. Joshi, "Review of Vehicle Engine Efficiency and Emissions," *SAE International Journal of Advances and Current Practices in Mobility,* vol. 2, pp. 2479-2507, 2020.

[4] W. Mitianiec, "Assesment of Total Efficiency in Adiabatic Engines," *IOP Conference Series: Materials Science And Engineering,* vol. 148, pp. 12080-12089, 2016.

[5] G. Z. Tang, B. C. Du and T. Deng, "Improvement of the Air-Cooled System on an Engine Cylinder Head and its Analysis," *Advances in Mechanical Engineering,* vol. 9, pp. 1-10, 2017.

[6] G. Eifler and T. Buck, "Thermosiphon Cooling," *MTZ Worldwide,* vol. 70, pp. 4-12, 2009.

[7] T. Mitchell, M. Salah, J. Wagner and D. Dawson, "Automotive Thermostat Valve Configurations: Enhanced Warm-Up Performance," *Journal of Dynamic Systems Measurement and Control,* vol. 131, pp. 44501-44508, 2009.

[8] D. Bjork and M. Gollin, "Comparative Performance of Ethylene Glycol/Water and Propylene Glycol/Water Coolant in Automotive Radiators," *SAE Technical Papers 960372,* 1996.

[9] Å. Melinder, "Thermophysical Properties of Aqueous Solutions Used as Secondary Working Fluids," *Doctoral Thesis at Royal Institute of Technology,* 2007.

[10] Tridon Australia LLC, "Tridon Radiator Cap Range Specification Sheet," Silverwater (NSW), 2020.

[11] F. Leach, G. Kalghatgi, R. Stone and P. Miles, "The Scope For Improving the Efficiency and Environmental Impact of Internal Combustion Engines," *Transportation Engineering,* vol. 1, pp. 5-22, 2020.

[12] S. Song and H. Zhang, "Performance Study for Miller Cycle Natural Gas Engine Based on GT-Power," *Journal Of Clean Energy Technologies,* vol. 3, pp. 351-355, 2015.

[13] M. De Cesare, N. Cavina and L. Paiano, "Technology Comparison for Spark Ignition Engines of New Generation," *SAE International Journal of Engine,* vol. 10, pp. 2513-2534, 2017.

[14] R. K. Raman, Y. Dewang and J. Raghuwanshi, "A Review on Applications of Computational Fluid Dynamics," *International Journal of LNCT,* vol. 2, pp. 137-143, 2018.

[15] R. B. Bird, W. E. Stewart and E. N. Lightfoot, Transport Phenomena, New York: John Wiley & Sons, Inc., 1960.

[16] C. J. Chadwell and M. Walls, "Analysis of a SuperTurbocharged Downsized Engine Using 1D CFD Simulation," *SAE Technical Paper 2010-01-1231,* 2010.

[17] M. A. Mashkour and M. H. Ibraheem, "3D - CFD Heat Transfer Simulation within Spark Ignition Engine," *Journal of the University of Kerbala,* vol. 17, pp. 64-88, 2019.

[18] X. C. Chun and C. H. Muk, "A Computational Fluid Dynamics Study of the Swirl Generation Analysis in Four-Stroke Direct Injection Engine," *Journal of Applied Mechanical Engineering,* vol. 5, pp. 5-10, 2016.

[19] A. Shingare and N. Totla, "Simulation of jacket cooling of a liner of four cylinder diesel engine for genset application," *International Engineering Research Journal,* vol. Special Issue, pp. 1276-1283, 2016.

[20] A. W. Date, Introduction to Computational Fluid Dynamics, Cambridge (UK): Cambridge University Press, 2005.

[21] ANSYS®, Inc., "ANSYS® Fluent® 2020 R2 Theory Guide," [Online]. Available: https://ansyshelp.ansys.com/account/secured?returnurl=/Views/Secured/corp/v202/en/flu_th/flu_th.html. [Accessed 16 November 2020].

[22] C. D. Argyropoulos and N. C. Markatos, "Recent Advances on the Numerical Modelling of Turbulent Flows," *Applied Mathematical Modelling,* vol. 39, pp. 693-732, 2015.

[23] ANSYS®, Inc., "About ANSYS," [Online]. Available: https://www.ansys.com/about-ansys. [Accessed 2 January 2021].

[24] ANSYS®, Inc., "Acquisitions & Partnerships: 2006," [Online]. Available: https://investors.ansys.com/company-information/acquisitions-and-partnerships/. [Accessed 8 January 2021].

[25] "Honda CB125R - Technical Specifications," [Online]. Available: https://www.honda.es/motorcycles/range/street/cb125r-2018/specifications.html#/. [Accessed 30 October 2020].

[26] P. Magryta, K. Pietrykowsky, M. Bialy and T. Tulwin, "CFD numerical simulation of the indirect cooling system of an internal combustion engine," *Combustion Engines,* vol. 170, pp. 8-18, 2017.

[27] "Bike Parts Honda: Honda genuine spare parts catalogue," [Online]. Available: https://www.bike-parts-honda.com/honda-motorcycle/125-MOTO/CBF/2018/CBF125NAJ/Frame/RADIATOR/100048/F_41/2/32229. [Accessed 30 October 2020].

[28] ANSYS®, Inc., "ANSYS® Meshing 2020 R2 User's Guide," [Online]. Available: https://ansyshelp.ansys.com/account/secured?returnurl=/Views/Secured/prod_page.html?pn=Meshing&prodver=20.2&lang=en. [Accessed 31 October 2020].

[29] P. M. Knupp, "Remarks On Mesh," in *45th AIAA Aerospace Sciences Meeting and Exhibit*, Reno (NV), 2007.

[30] ANSYS®, Inc., "ANSYS® Fluent® 2020 R2 User's Guide," [Online]. Available: https://ansyshelp.ansys.com/account/secured?returnurl=/Views/Secured/corp/v202/en/flu_ug/flu_ug.html. [Accessed 5 November 2020].

[31] *ASTM D3306-20. Standard Specification for Glycol Base Engine Coolant for Automobile and Light-Duty Service,* West Conshohocken (PA): ASTM International, 2020.

[32] T. K. Jack and M. M. Ojapah, "Water-Cooled Petrol Engines: A Review of Considerations in Cooling Systems Calculations with Variable Coolant Density and Specific Heat," *International Journal of Advances in Engineering & Technology,* vol. 6, pp. 659-667, 2013.

[33] "Santa Clara University Engineering Center: Mold Cooling Design Considerations," [Online]. Available: https://www.dc.engr.scu.edu/cmdoc/dg_doc/develop/design/cooling/31000005.htm. [Accessed 18 November 2020].

[34] H. Chen, Y. Hu, Y. Hu, X. Gong and Z. Zhao, "Modeling and Optimization Contron for an Engine Electrified Cooling System to Minimize Fuel Consumption," *IEEE Access,* vol. 7, pp. 72 914-72 927, 2019.

[35] R. I. Abdul-Jalal, "Engine thermal management with model predictive control," *Doctoral Thesis at Loughborough University,* 2016.

[36] G. Singh and K. Howden, "Achieving and Demonstrating Vehicle Technologies: Engine Fuel Efficiency Milestones," in *2010 DOE Vehicle Technologies and Hydrogen Programs Annual Merit Review and Peer Evaluation Meetin*, Washinton D.C., 2010.

[37] G. Thomas, "Overview of Storage Development. DOE Hydrogen Programe," in *US DOE Hydrogen Program 2000 Annual Review*, San Ramon (California), 2000.

[38] T. K. Hayes, R. A. White and J. E. Peters, "Combustion Chamber Temperature and Instantaneous Local Heat Flux Measurements in a Spark Ignition Engine," *SAE Technical Paper 930207,* 1993.

[39] P. Merati, C. Davis, K.-H. Chen and J. P. Johnson, "Underhood Buoyancy Driven Flow - An Experimental Study," *Journal of Heat Transfer,* vol. 133, pp. 82502_1-82502_9, 2011.

[40] O. Levenspiel, "Chapter 9. The Three Mechanisms of Heat Transfer: Conduction, Convection and Radiation," in *Engineering Flow and Heat Exchange, Revised Edition*, New York (New York), Plenum Press, 1998, pp. 169-196.

[41] Perry's Chemical Engineer Handbook 7th edition, New York (New York): McGraw Hill, 1997, pp. 337-374.

[42] R. D. Burke, A. J. Lewis, S. Akehurst, C. J. Brace, I. Pegg and R. Stark, "Systems Optimisation of an Active Thermal Management System During Engine Warm-Up," *Journal of Automotive Engineering,* vol. 226, pp. 1365-1379, 2012.

[43] A. Haury and J. Volkering, "Modelisation of the Engine Coolant Warming-Up Behavior," *Master's Thesys at Chalmers University of Technology,* 2011.

[44] K. Robinson, J. G. Hawley, G. P. Hammond and N. J. Owen, "Convective Coolant Heat Transfer in Internal Combustion Engines," *Journal of Automotive Engineering,* vol. 217, pp. 133-146, 2003.

[45] H. Punekar and S. Das, "Numerical Simulation of Subcooled Nucleate Boiling in Cooling Jacket of IC Engine," in *SAE World Congress & Exhibiton*, 2013.

[46] E. Jiaqiang, Z. Zhiquing, T. Zhengfang, Z. Wei, H. Wenyu, H. Dandan and J. Yu, "Effect Analisys on Flow and Boiling Heat Transfer Performance of Cooling Water-Jacket of Bearing in the Gasoline Enigne Turbocharger," *Applied Thermal Engineering,* vol. 130, pp. 754-766, 2018.

[47] J. Martins, A. Monteiro and J. Barbosa, "18th International Congress of Mechanical Engineering: Engine Design Using Rapid Prototyping Techniques," in *Proceedings of COBEM*, Ouro Preto (Mg).

[48] A. R. Andsaler, A. Khalid, H. Ramsy and N. Jaat, "A Review Paper on Simulation and Modeling of Combustion Characteristics Under High Ambient and High Injection of Biodiesel Combustion," *Applied Mechanics and Materials,* vol. 773, pp. 580-584, 2015.

ACRONYMS

CFD	Computational Fluid Dynamics
CI	Compression-ignition
EG	Ethylene glycol
HTC	Heat transfer coefficient
IC	Internal combustion
ICE	Internal combustion engine
SI	Spark-ignition
W	Water
WAFT	Wall-adjacent fluid temperature

APPENDICES

APPENDIX 1: THERMOPHYSICAL PROPERTIES OF EG-W MIXTURES

Experimental values for the thermophysical properties of 50% $^{V}/_{V}$ mixtures of ethylene glycol and water were obtained from the work of Å. Melinder [9] and were then adjusted to suitable expressions for their use on ANSYS® Fluent® simulations. The optimal correlation for each thermophysical property was extracted from Perry's Chemical Engineer Handbook [41]. Unless otherwise stated all temperatures are in Celsius.

Thermal conductivity (k):

$$k\ [W/(m\cdot ºC)] = -1.6277\cdot 10^{-6}\ T^2 + 6.8664\cdot 10^{-4}\ T + 3.5427\cdot 10^{-1}\ \{R^2 = 0.9999\}$$

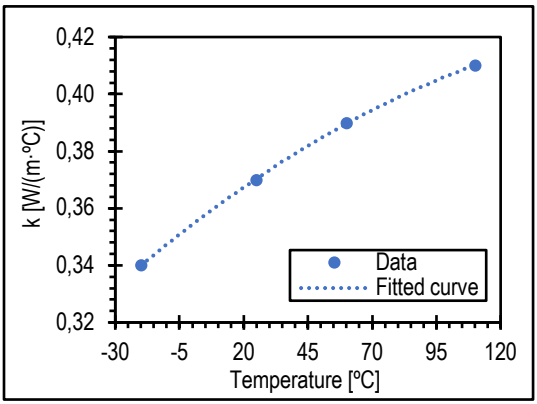

Figure A1.1. Thermal conductivity experimental values as a function of temperature and their recommended fit.

Density (ρ):

$$\rho\ [kg/m^3] = -1.1972 \cdot 10^{-3} \cdot T^2 - 4.8183 \cdot 10^{-1} \cdot T + 1.0890 \cdot 10^3 \quad \{R^2 = 0.9988\}$$

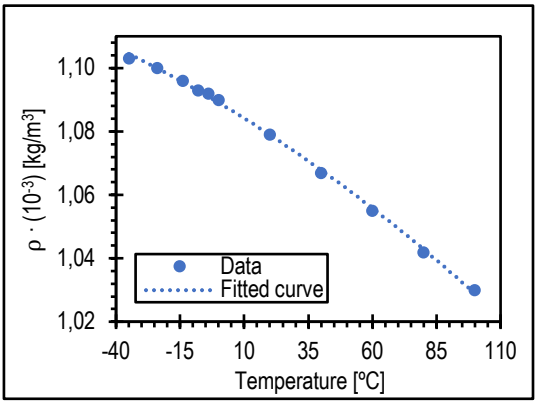

Figure A1.2. Density experimental values as a function of temperature and their recommended fit.

Dynamic viscosity (μ): since the correlation used is based on an Arrhenius thermokinetic equation, the temperature used is absolute (Kelvin):

$$\mu\ [kg/(m \cdot s)] = 5.7480 \cdot 10^{-7} \cdot \exp\left(2.5647 \cdot 10^3 \cdot T^{-1}\right) \quad \{R^2 = 0{,}9891\}$$

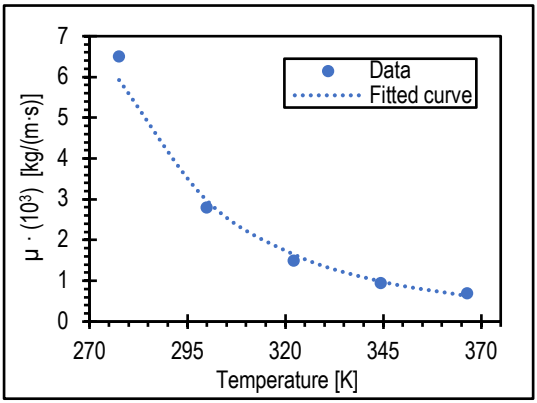

Figure A1.3. Dynamic viscosity experimental values as a function of temperature and their recommended fit.

Specific heat (C_P):

$$C_P\ [J/(kg{\cdot}°C)] = 3.0658 \cdot T + 3.4117 \cdot 10^3 \quad \{R^2 = 1.000\}$$

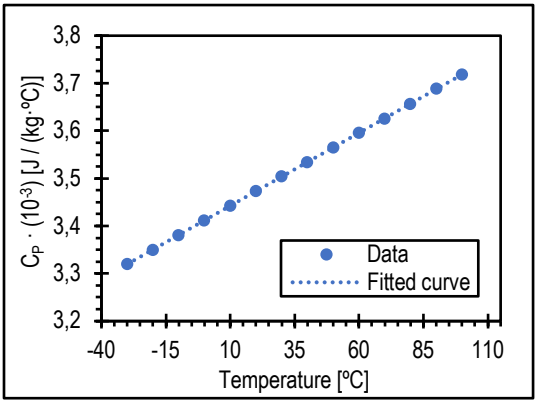

Figure A1.4. Specific heat experimental values as a function of temperature and their recommended fit.

Bubble pressure (P_B): as opposed to all previous properties, bubble pressure for different temperatures was obtained from simulations on AspenTech's Aspen Plus V10® using the NRTL interaction model. No fitted curve was necessary for the development of this work.

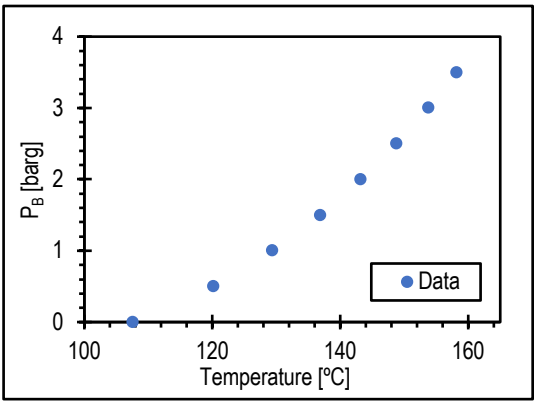

Figure A1.5. Relative bubble pressure estimated values as a function of temperature and their recommended fit.

APPENDIX 2: OTHER VIEWS OF THE ENHANCED COOLING JACKETS

In the following appendix section, other views for the studied system are presented for clarification if needed. As for all the diagrams in this work, the views presented in this appendix are drawn to scale. Color coding for all diagrams is as follows:

Inlet Outlet Cooling Fluid Baffle

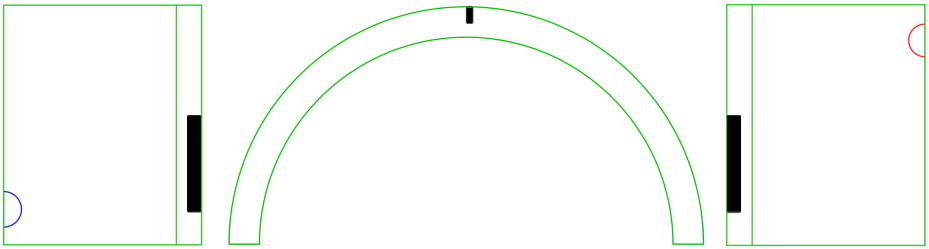

Figure A2.1. Inlet side (left), top (center) and outlet side (right) views for the system with a vertical baffle (VB).

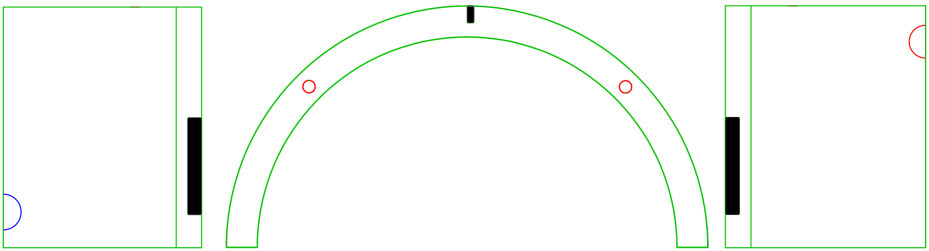

Figure A2.2. Inlet side (left), top (center) and outlet side (right) views for the system with a vertical baffle and additional outlets (VBAO).

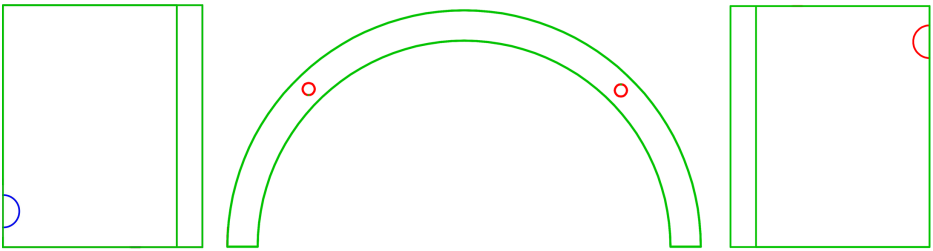

Figure A2.3. Inlet side (left), top (center) and outlet side (right) views for the system with only additional outlets (AO).

APPENDIX 3: DISCARDED PROTOTYPES

In the following appendix section, the geometrical models for the discarded prototypes and their WAFT contour and trajectory streamlines combined representations are shown. As for all the diagrams in this work, the views presented in this appendix are drawn to scale. Color coding for all diagrams is as follows: Inlet Outlet Cooling Fluid Baffle

Discarded prototype 1: this was the first prototype analyzed. A baffle with a height of 1/3 of that of the cooling jacket was placed on the inner wall. Its prominence was set as 1 mm and it pointed towards the main WAFT hotspot in the inner wall to try to direct the flow to that area. No additional outlets were used. It was discarded because Its low prominence and its position (on the inner wall) it caused very little effect on the WAFT values (and caused hotspots around it)

Figure A3.1. Inlet side (left), outside (center) and outlet side (right) of the first discarded prototype.

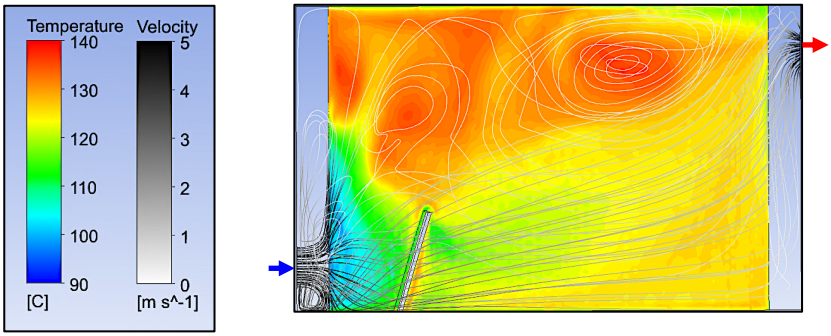

Figure A3.2. WAFT contour and trajectory streamlines combined representation for the first discarded prototype.

Discarded prototype 2: the baffle was enlarged with respect to the previous (1.0 mm of prominence and 2/3 of the cooling jacket height) but was it still positioned on the inner wall with the same orientation. No additional outlets were used. This prototype was discarded because it was found that baffles on the inner wall had little effect on the global flow characteristics due to the fact that the flow was concentrated on the outer wall. The effects of baffles located on the inner wall were found to be more localized and less intense than for baffles located on the outer wall.

Figure A3.3. Inlet side (left), outside frontal (center) and outlet side (right) of the second discarded prototype.

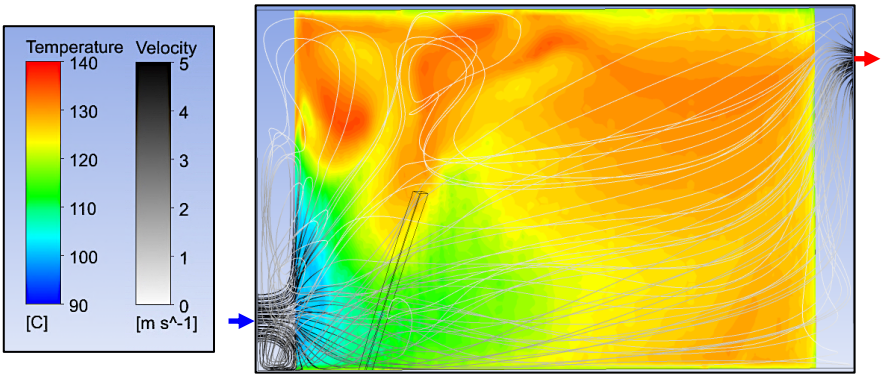

Figure A3.4. WAFT contour and trajectory streamlines combined representation for the second discarded prototype.

Discarded prototype 3: the baffle was located on the outer wall and was given more prominence (3 mm). It was now centered, to try to intercept the short-circuit found on the simple system analyzed on section 4.1.1. No additional outlets were used. It was abandoned because since it was located on the bottom part it deprived the bottom part of sufficient flow and created a hotspot behind it in the direction of the flow. This was one of the predecessors of the VB and VBAO prototypes and allowed for the optimization of the vertical position of the baffle.

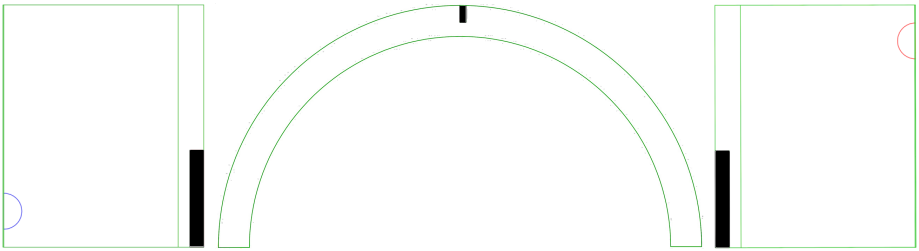

Figure A3.5. Inlet side (left), top (center) and outlet side (right) of the third discarded prototype.

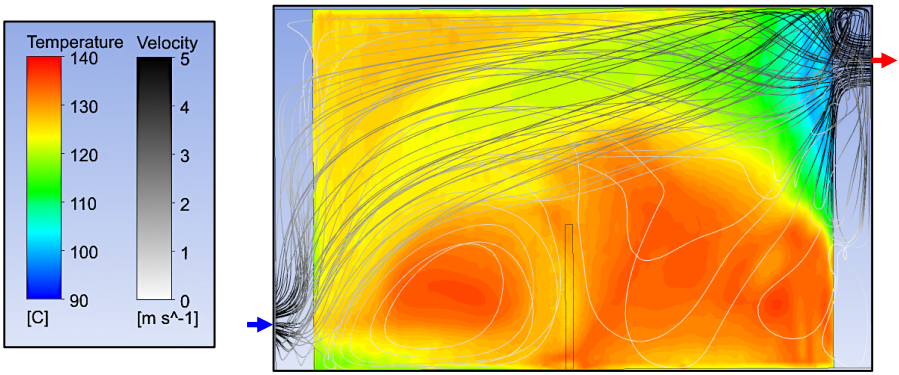

Figure A3.6. WAFT contour and trajectory streamlines combined representation for the third discarded prototype.

Discarded prototype 4: as the previous discarded prototype this one is also a predecessor of the VB and VBAO prototypes. The baffle was now centered in height to avoid the hotspot creation caused by positioning it on the bottom part of the cooling jacket. This prototype was discarded because in this position, the main short-circuit present in the system bypassed the baffle by flowing under it. The VB and VBAO prototypes are an evolution of this discarded prototype with their respective baffles located in an intermediate position between the one found on this and the discarded prototype 3. In that intermediate position interception of the short-circuit was found to be optimal.

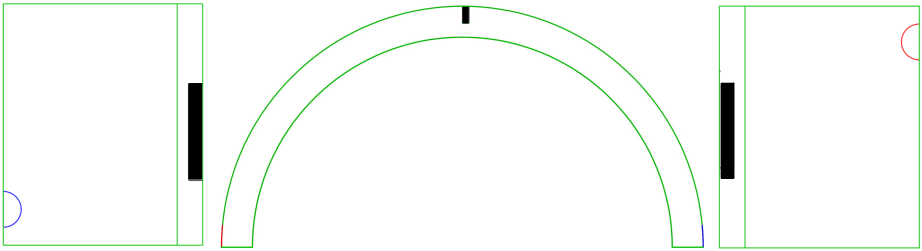

Figure A3.7. Inlet side (left), top (center) and outlet side (right) of the fourth discarded prototype.

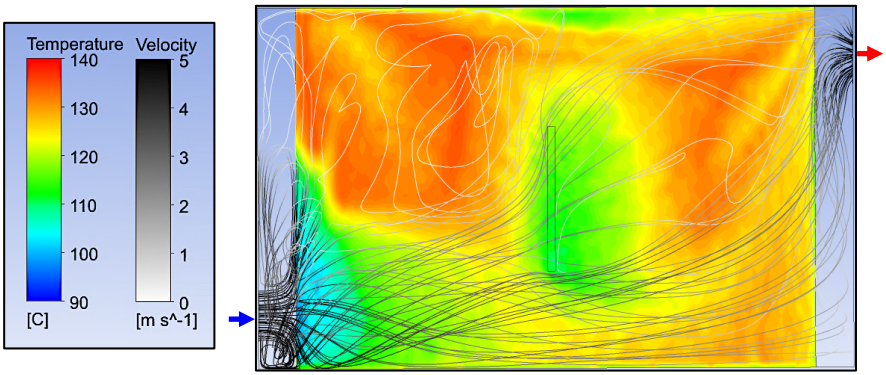

Figure A3.8. WAFT contour and trajectory streamlines combined representation for the fourth discarded prototype.